processes

MDPI

Review

Recent Advances in the Photocatalytic Degradation of Phenol over Bi-Based Oxide Catalysts

Zhangpei Liu [1], Maosheng Qian [1], Xiaomeng Cheng [2,*] and Zhiming Liu [1,*]

[1] State Key Laboratory of Chemical Resource Engineering, Beijing University of Chemical Technology, Beijing 100029, China
[2] Institute of Geophysical & Geochemical Exploration, Chinese Academy of Geological Sciences, Langfang 065000, China
* Correspondence: cxiaomeng@mail.cgs.gov.cn (X.C.); liuzm@mail.buct.edu.cn (Z.L.); Tel.: +86-10-64412787 (Z.L.)

Abstract: Wastewater containing phenolic organic compounds, such as phenol, produced during industrial manufacturing processes, poses a significant threat to aquatic ecosystems and crops. Photocatalytic technology is considered the most promising approach to water treatment due to its efficiency and eco-friendly advantages. Compared to other photocatalysts, Bi-based oxides are more efficient due to their unique layered structure, which allows for photocatalytic reactions to occur between layers. This review introduces the synthesis methods of various bismuth-based multi-element oxides and their efficiency in the photocatalytic decomposition of phenol. The effects of elemental doping, defect introduction, and heterojunction construction on the catalytic performance and structure of Bi-based oxides are discussed. The mechanisms for the photocatalytic degradation of phenol over different materials are also summarized and discussed.

Keywords: phenol; photocatalytic degradation; bismuth-based photocatalysts; heterojunction

Citation: Liu, Z.; Qian, M.; Cheng, X.; Liu, Z. Recent Advances in the Photocatalytic Degradation of Phenol over Bi-Based Oxide Catalysts. *Processes* **2024**, *12*, 1799. https://doi.org/10.3390/pr12091799

Academic Editors: Jan Derco, Andreja Žgajnar Gotvajn and Angelika Kassai

Received: 28 July 2024
Revised: 9 August 2024
Accepted: 15 August 2024
Published: 24 August 2024

1. Introduction

Recently, the acceleration of industrialization has led to wastewater from industrial production processes exerting immense pressure on the environment [1]. Particularly, phenolic organic pollutants, such as phenol, with high chemical stability and strong biological toxicity, pose significant challenges for effective removal from receiving water bodies, thereby causing severe harm to both the ecosystem and human health [2,3]. Therefore, the effective treatment of phenolic wastewater is considered a fundamental and challenging task.

Currently, treatments for phenolic wastewater primarily include chemical, biological, physical methods, membrane filtration, and photocatalytic technology [4–6]. Among them, photocatalytic technology is regarded as an effective method for addressing wastewater pollution. A variety of photocatalysts have been developed and extensively studied. Compared with traditional pollutant treatment technologies, photocatalytic technology offers some advantages, including using sunlight for its driving energy, a renewable resource that ensures no energy shortage [7]. No chemicals are needed for this process, and it generates potent oxidative free radicals that can completely mineralize pollutants into carbon dioxide and water; furthermore, the photocatalysts are non-toxic and reusable, thereby reducing the costs associated with pollutant treatment [8].

Recent years, bismuth (Bi)-based photocatalysts have attracted considerable attention, primarily due to their well-dispersed Bi 6s orbitals. These orbitals result in a narrow bandgap, enabling efficient absorption of visible light and excellent catalytic activity on the visible spectrum [9–13]. Moreover, the structure of layered Bi-based catalysts, consisting of alternating Bi-O layers and transition metal oxide layers, facilitates weak van der Waals interactions. This structure allows for elemental doping through replacement or insertion,

which alters the composition and charge balance of semiconductors, thereby regulating its absorption ability and enhancing the properties of photogenerated carriers [14–16]. Additionally, the construction of heterostructures can efficiently separate photogenerated carriers, minimize recombination losses, enhance the migration and reaction capabilities of photogenerated carriers, thereby significantly improving the efficiency and stability of Bi-based photocatalysis [17–21]. In this study, recent research on Bi-based photocatalysts and their heterojunction composites in the degradation of phenol is reviewed. The goal is to provide a detailed discussion on the various design approaches for Bi-based photocatalysts and their mechanisms in phenol degradation, thus shedding light on the design of more active photocatalysts for the degradation of phenol.

2. Basics of Photocatalytic Degradation of Pollutants

Within band theory, the energy levels of semiconductor materials are divided into two distinct regions: the valence band (VB) and the conduction band (CB). The energy difference between these bands is known as the bandgap or forbidden band width (E_g). As a photocatalytic material is irradiated with ultraviolet or visible light, photons with energy equal to or greater than the forbidden bandwidth are absorbed in its bulk phase. Within femtoseconds, the semiconductor undergoes photoexcitation; electrons transition from the VB to the CB, simultaneously causing holes due to electrons absence. Following the relaxation process (approximately a picosecond), most electrons and holes recombine, producing a fluorescence effect and releasing energy, while others migrate from the bulk to the surface of the material. At this stage, photogenerated carriers, specifically electrons (e^-) and holes (h^+), are formed [22]. In the aqueous phase, the electron and hole pairs on the surface of the photocatalytic material, excited by light, react with O_2 and H_2O adsorbed on the surface to produce potent oxidative free radicals, namely $\cdot O_2^-$ and ·OH. Owing to the potent oxidizing properties of these active free radicals, they can oxidize waterborne pollutants into CO_2 and H_2O. Detailed reaction processes and the corresponding schematics are illustrated below (Figure 1).

$$\text{Photocatalysts} + hv \rightarrow \text{Electron } (e^-) + \text{hole } (h^+) \quad (1)$$

$$\text{Electron } (e^-) + \text{hole } (h^+) \rightarrow \text{Recombination} \quad (2)$$

$$\text{Electron } (e^-) + O_2 \rightarrow O_2^- \quad (3)$$

$$\text{hole } (h^+) + H_2O \rightarrow OH + H^+ \quad (4)$$

$$\text{hole } (h^+) + \cdot O_2^- \rightarrow {}^1O_2 \quad (5)$$

$$O_2^- + \cdot OH + {}^1O_2 + \text{Pollutants} \rightarrow CO_2 + H_2O \quad (6)$$

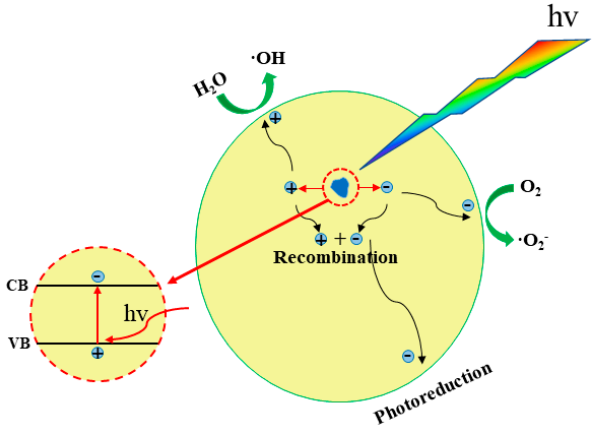

Figure 1. A schematic picture of the photocatalytic process and the degradation of pollutant.

3. Bi-Based Oxide Photocatalysts in Phenol Degradation

Bi is a p-block element that belongs to group VA of the sixth period on the periodic table. Its outermost electron shell consists of $6s^2 6p^3$ electrons, with two electrons in the 6s orbital and three in the 6p orbital. The Bi-based multicomponent oxides' photocatalytic activities are directly influenced by their electronic and crystallographic properties. The VB of Bi-based multicomponent oxides result from the hybridization of O 2p and Bi 6s orbitals. The distortion of the Bi 6s orbitals' lone pair can cause significant overlap with the O 2p orbitals, facilitating carrier migration and reducing the bandgap width [23]. Consequently, the bandgap width of these oxides is typically less than 3.0 eV. Given the relative stability of Bi^{3+}, much of the research focuses on compounds containing Bi^{3+}, such as Bi_2O_3, $BiVO_4$, Bi_2MO_6 (M = Mo, W), $BiFeO_3$, and BiOX (X = Cl, Br, I), as depicted in Figure 2.

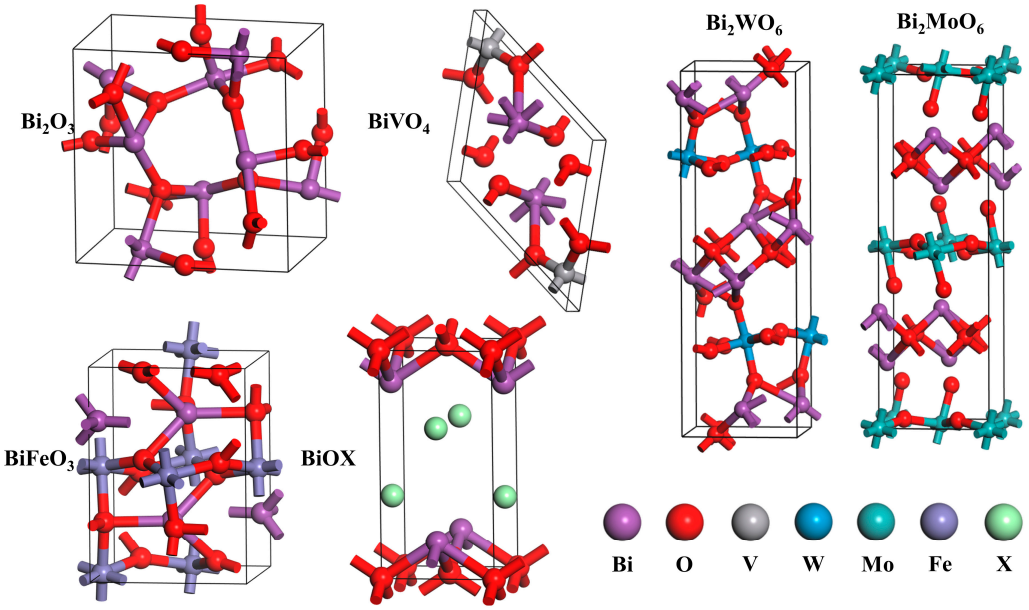

Figure 2. Crystal structures of several Bi-based polyoxides.

Owing to their exceptional redox capabilities, efficient solar energy utilization, effective separating photogenerated carriers, and superior photocatalytic performance, the aforementioned Bi-based multicomponent oxides were extensively studied in the degradation of miscellaneous pollutants, including organic phenols [24], dyes [25], antibiotics [26], and heavy metals [27]. This section introduces the application of Bi-based oxide photocatalysts for the degradation of phenol in the wastewater.

3.1. Bi_2O_3

Bi_2O_3, with a bandgap width of 2.1–2.8 eV, exhibits good responsiveness to visible light. Bi_2O_3 exists in four phases: monoclinic (α-Bi_2O_3), tetragonal (β-Bi_2O_3), body-centered cubic (γ-Bi_2O_3), and face-centered cubic (δ-Bi_2O_3). Among these, α-Bi_2O_3 and δ-Bi_2O_3 are stable, whereas the others are metastable [28]. β-Bi_2O_3 exhibits superior photocatalytic activities compared to α-Bi_2O_3, owing to the lower bandgap energy and higher light absorption capability in the visible light region [9]. However, because β-Bi_2O_3 has a metastable structure, it can easily transform into α-Bi_2O_3 under certain conditions, making the controlled synthesis and catalytic stability of β-Bi_2O_3 challenging.

Li et al. [29] prepared pure Bi_2O_3 via a simple sol–gel method, which, upon calcination, could form oxygen vacancies serving as photocatalytic active sites. Within 240 min, the degradation efficiency of phenol was merely 31%. Meng et al. [30] synthesized α-Bi_2O_3 through a co-precipitation method. The irregular microparticle-shaped α-Bi_2O_3, with a surface area of just 10.1 $m^2 \cdot g^{-1}$, resulted in limited active sites for pollutant adsorption, achieving a degradation efficiency of 48% for phenol within 60 min. Liang et al. [9] syn-

thesized Bi_2O_3 crystals with varied morphologies via a chemical bath deposition method by controlling the pH (Figure 3a,b). They employed a sputter coating method to modify the Bi_2O_3 crystals, synthesizing α-Bi_2O_3 and β-Bi_2O_3. It was demonstrated that a higher pH of the solution facilitated the evolution of the α-Bi_2O_3 phase. Wu et al. [31] prepared α-Bi_2O_3, β-Bi_2O_3, and γ-Bi_2O_3 via hydrothermal treatment followed by calcination. Among these, β-Bi_2O_3 had a degradation efficiency of up to 97% for phenol after 90 min of sunlight exposure, significantly outperforming the other two phases of Bi_2O_3 in terms of photodegradation efficiency.

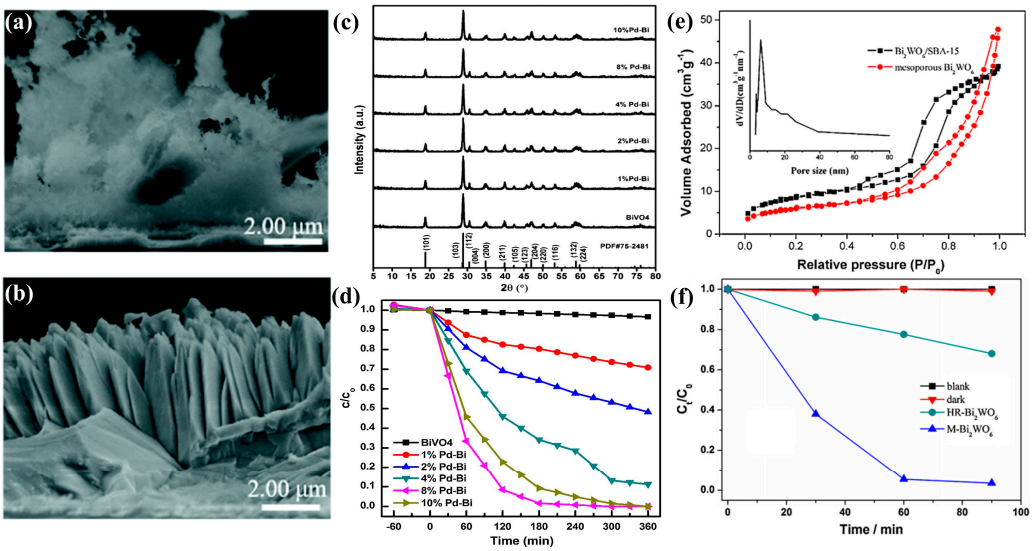

Figure 3. SEM images of (**a**) pH10-Bi_2O_3, (**b**) pH13-Bi_2O_3. Reprinted with permission from Ref. [9]. Copyright 2020 Royal Society of Chemistry. (**c**) XRD patterns of different ratio of pd-doping $BiVO_4$, (**d**) Degradation activity of phenol solutions under UV-Vis irradiation with $BiVO_4$ photocatalysts. Reprinted with permission from Ref. [32]. Copyright 2017 Elsevier. (**e**) Nitrogen adsorption and desorption curve of mesoporous Bi_2WO_6. (**f**) Efficiency of photocatalytic degradation of phenol with different Bi_2WO_6 Reprinted with permission from Ref. [33]. Copyright 2011 Elsevier.

3.2. BiVO4

$BiVO_4$ primarily exists in three crystalline phases: monoclinic scheelite (M-S $BiVO_4$), tetragonal scheelite (T-S $BiVO_4$), and tetragonal zircon (T-Z $BiVO_4$) [34]. Among these, M-S $BiVO_4$ was extensively studied for the superior photocatalytic performance, due to the relatively finite bandgap (E_g = 2.4 eV) and the electron modulation of the Bi 6s and hybrid Bi 6s-O 2p orbitals to the V 3d orbital conduction band [10]. Compared with M-S $BiVO_4$, T-S $BiVO_4$ exhibits lower photocatalytic activity for the wider bandgap of 2.9 eV, limiting its responsiveness in the visible light region. T-Z $BiVO_4$ displays the lowest photocatalytic activity; however, its relatively simple preparation conditions make it the easiest to synthesize among the three phases [35]. Moreover, T-Z $BiVO_4$, possessing a high degree of crystal symmetry, facilitates the formation of coherent interfaces, rendering it particularly valuable for exploration in polycrystalline materials. Therefore, effective control over the crystal structure of $BiVO_4$ can maximize its catalytic activity. Monoclinic phase M-S $BiVO_4$ was prepared by Xie et al. [36] via a solution stirring and calcination method, achieving a photocatalytic effect on phenol of up to 52% within 180 min. Sun et al. [37] found that, during the preparation of monoclinic phase M-S $BiVO_4$ under different pH conditions utilizing a solvothermal method, when the precursor solution was adjusted to pH 11, it achieved a conversion of phenol of 54% within 300 min. As shown in Figure 3d, Meng et al. [32] prepared pure $BiVO_4$ through the hydrothermal method, achieving a low degradation efficiency of phenol, merely 3.4% within 360 min. The removal rate of phenol was greatly improved after palladium (Pd) was introduced in $BiVO_4$. The maximum

degradation rate of phenol can reach 100%. According to the XRD pattern (Figure 3c), the crystal structure of $BiVO_4$ was not destroyed after Pd was deposited by light.

3.3. Bi_2WO_6

Bi_2WO_6 is a simple Aurivillius-type layered compound, characterized by the alternate stacking of $[Bi_2O_2]^{2+}$ lamellar structures and WO_4. $[Bi_2O_2]^{2+}$ layers and WO_4 layers are connected by shared oxygen atom vertices, resulting in weak van der Waals forces. Bi_2WO_6 exhibits multiple crystal structures, including orthorhombic, monoclinic, and tetragonal phases, with structural differences primarily due to the rotation angle of the WO_4 layer and the degree of dislocation of the $[Bi_2O_2]^{2+}$ layer [38]. Bi_2WO_6 is classified as a wide-bandgap photocatalyst (2.5–2.8 eV). The positions of its conduction band minimum (CBM) and valence band maximum (VBM) are 0.24 eV and 3.12 eV, respectively [39], which are relatively high energy levels that effectively suppress photogenerated carrier recombination. Simultaneously, owing to the layered structure of Bi_2WO_6, photocatalytic reactions primarily occur between layers, where the $[Bi_2O_2]^{2+}$ layer serves as the receptor for photogenerated electrons and the WO_4 layer as the carrier for photogenerated holes. This enables the effective separation and migration of carriers, therefore significantly enhancing photocatalytic efficiency.

Sattari et al. [40] successfully synthesized orthorhombic Bi_2WO_6 through the hydrothermal method, achieving a degradation efficiency of 34% for phenol within 120 min. The morphology of Bi_2WO_6 is nanosheet-like, with limited photocatalytic active sites, resulting in a lower degradation efficiency of phenol. Fu et al. [11] synthesized tetragonal Bi_2WO_6 using the hydrothermal method, which self-assembled from nanoplates into flower-like microspheres, yielding a surface region of 39.7 $m^2 \cdot g^{-1}$ and offering abundant adsorption sites for pollutants. After visible light irradiation for 40 min, the conversion of phenol increased to 56.5%. Sun et al. [33] prepared Bi_2WO_6 using SiO_2 as the hard template. As shown in Figure 3e, the sample maintains the mesoporous structure of SiO_2. Under visible light irradiation, 97% of phenol is degraded within 60 min, as depicted in Figure 3f, demonstrating remarkable photocatalytic performance. In contrast, the conversion of phenol by orthorhombic Bi_2WO_6 synthesized using the common hydrothermal method stands at only 32%. Therefore, the active sites of photocatalytic degradation of phenol over Bi_2WO_6 are predominantly located on the surface of the mesoporous structure.

3.4. Bi_2MoO_6

Bismuth molybdate (Bi_2MoO_6) possesses a perovskite-layered structure, analogous to that of bismuth tungstate (Bi_2WO_6). The normal state of Bi_2MoO_6 is γ-Bi_2MoO_6, characterized by the optional heaping of $[Bi_2O_2]^{2+}$ layers and $[MoO_4]^{2-}$ octahedral layers. The resulting layered structure not only endows Bi_2MoO_6 with the unique advantages of a two-dimensional nanostructure but also facilitates the separation and transmission of carriers by the internal electric field (IEF) formed between the layers. The bandgap of Bi_2MoO_6, 2.5–2.8 eV, enables a firm response in the visible light area. In addition to the unique layered structure and appropriate bandgap, the non-toxicity, low cost, and excellent thermal and chemical inertness of Bi_2MoO_6 further promote its application in environmental remediation.

Fu et al. [12] reported a solvothermal method for preparing pure Bi_2MoO_6, followed by calcination at 250 °C to modify the surface oxygen vacancies. The EPR signal of oxygen vacancies is clearly visible in Figure 4a. At 180 min of visible light irradiation, the degradation virtue of phenol by pure Bi_2MoO_6 stood at only 4.8%. However, calcination results in lattice contraction in Bi_2MoO_6, resulting in the formation of oxygen vacancies on its surface. Under the same conditions, this increased the degradation efficiency of phenol to 35%. Liu et al. [41] further optimized the preparation method used by Fu et al. by increasing the calcination temperature to 300 °C and extending the calcination time. This increase led to a degradation efficiency of phenol of 44% within 180 min, indicating that the calcination temperature may be a key factor in phenol degradation over Bi_2MoO_6. To

verify this hypothesis, Sun et al. [42] assessed the photocatalytic degradation of phenol in materials intended at different calcination temperatures. The material calcined at 450 °C showed excellent performance for phenol degradation (Figure 4b). Therefore, variations in the calcination temperature of Bi_2MoO_6 will produce different amounts of oxygen vacancies. Oxygen vacancies, serving as electron traps, effectively capture photogenerated electrons, facilitating the separation of photogenerated carriers. In the FTIR spectrum (Figure 4i), the 410–565 cm^{-1} and 730–850 cm^{-1} absorption bands correspond to the stretching vibrations of the Bi-O bond and the Mo-O bond, and the EDS energy spectrum (Figure 4j) shows a uniform distribution of Bi, Mo, O, and C in the selected region, which suggests the successful synthesis of Bi_2MoO_6. The absence of O atoms also reflects the formation of oxygen vacancies due to calcination [24]. Moreover, materials containing oxygen vacancies can generate another type of active free radical, $^1O_2$, enhancing the oxidative degradation of phenol [24].

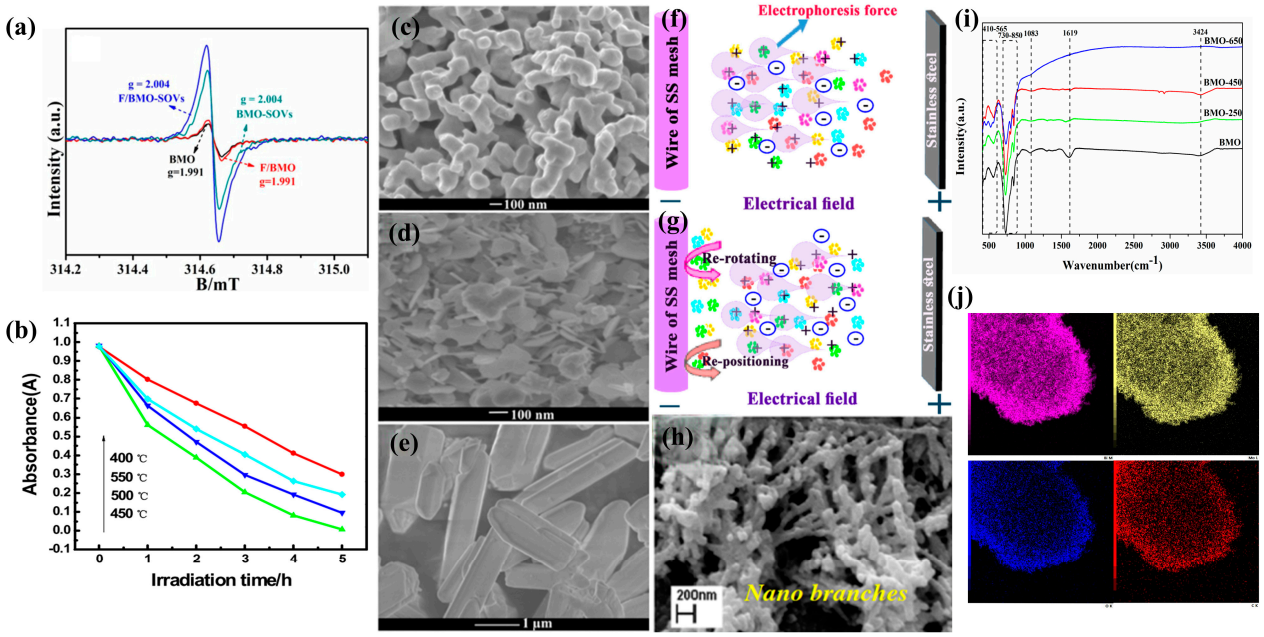

Figure 4. (**a**) EPR signal map of Bi_2MoO_6 and surface oxygen vacancies Bi_2MoO_6. Reprinted with permission from Ref. [12]. Copyright 2019 Elsevier. (**b**) Photocatalytic activity of Bi_2MoO_6 at different calcination temperatures. Reprinted with permission from Ref. [42]. Copyright 2019 Elsevier. (**c**–**e**) Different morphology of $BiFeO_3$ prepared by hydrothermal (HT-$BiFeO_3$), co-precipitation (CP-$BiFeO_3$) and sol-gel methods (SG-$BiFeO_3$). Reprinted with permission from Ref. [43]. Copyright 2022 Elsevier. Growth mechanism of $BiFeO_3$ film schematic diagram: (**f**) The ion clusters are moved by electrophoretic forces. (**g**) The ion clusters are repositioned and deposited on the electrode surface. (**h**) Growth of forest-like $BiFeO_3$ nano branches on the carrier surface. Reprinted with permission from Ref. [44]. Copyright 2019 Elsevier. (**i**) FT-IR spectrum of Bi_2MoO_6. (**j**) The EDS spectrum of BMO-450. Reprinted with permission from Ref. [24]. Copyright 2022 Elsevier.

3.5. $BiFeO_3$

Perovskite bismuth ferrite ($BiFeO_3$), akin to other Bi-based multicomponent oxides, is formed through the alternating stacking of [FeO_6] octahedra and $[Bi_2O_2]^{2+}$ layers. It belongs to the rare class of single-phase multiferroic semiconductors [45]. Its bandgap ranges from 2.0 to 2.7 eV, categorizing it as a narrow-bandgap semiconductor [46]. The CBM and VBM consist of Bi 6p/O 2p and O 2p/Fe 3d orbitals, respectively. The extent of hybridization among orbitals determines the bandgap and the light absorption spectrum of $BiFeO_3$ [47]. The photocatalytic efficiency of $BiFeO_3$ is primarily affected by factors such as its structural and morphological characteristics. Typically, morphologies featuring a

larger surface region and active sites, such as nanoparticles, nanoflowers, nanosheets, and nanoplates, increase the photocatalytic performance of $BiFeO_3$.

Mansingh et al. [48] synthesized nanosheet-shaped $BiFeO_3$ via a hydrothermal method. The photocatalytic degradation efficiency of phenol is 41% within 60 min; this relatively low efficiency was attributed to the agglomeration of pure $BiFeO_3$, which obscured active sites. Jaffari et al. [43] prepared $BiFeO_3$ particles with varied morphologies by three distinct synthesis routes (hydrothermal, co-precipitation, and sol–gel methods). HT-$BiFeO_3$, CP-$BiFeO_3$, and SG-$BiFeO_3$ were integrated, respectively (Figure 4c–e). All samples conformed to the rhombohedral structure of $BiFeO_3$, differing only in morphology. HT-$BiFeO_3$ exhibited a coral-like shape, CP-$BiFeO_3$ was sheet-like, and SG-$BiFeO_3$ displayed a rod-like structure. Over 120 min, the photocatalytic degradation efficiencies of phenol were 77.4%, 66.9%, and 98.95%, respectively. The highest performance of SG-$BiFeO_3$ was attributed to the modified separation efficiency of photo carriers due to the sol–gel method [45]. Based on these findings, Zargazi et al. [44] utilized sol electrophoretic deposition to synthesize a forest-like $BiFeO_3$ thin film. The synthesis mechanism and microscopic morphology are depicted in Figure 4f–h. This method not only yielded high-purity, uniform $BiFeO_3$ but also overcame the aging drawbacks associated with the sol–gel method. When phenol molality of 15, 30, 50, and 80 ppm was established, the observed half-lives were 27, 30, 54, and 120 min, respectively. The exceptional photocatalytic activity of $BiFeO_3$ thin film is attributed to the nano-branches on its surface that facilitate the diversion of photogenerated electrons.

3.6. BiOX

Bismuth halogen oxides (BiOX) are classified within the V-VI-VII group and possess a PbFCl-type structure. They are characterized by high chemical stability, non-toxicity, environmental friendliness, and robust corrosion resistance. As illustrated in Figure 2, their crystal structure results from the alternating arrangement of $[Bi_2O_2]^{2+}$ layers and double $[X]^-$ layers, influenced by van der Waals forces, with Bi and O in the $[Bi_2O_2]^{2+}$ layers linked by covalent bonds [13]. This layered structure, composed of cations and anions, affords ample space for the polarization of respective atoms and orbitals, extends the lifetime of photogenerated carriers, and facilitates the constitution of an IEF [49]. As depicted in Figure 5a, with an increasing atomic number of the halogen atom, the bandgap of BiOCl (E_g = 3.2 eV), BiOBr (E_g = 2.6 eV), and BiOI (E_g = 1.8 eV) progressively narrows. The valence band of BiOX primarily consists of O 2p orbitals and X np orbitals (n = 3, 4, 5 corresponding to X = Cl, Br, I), while CB comprises Bi 6p orbitals. The hybridization of Bi 6s and O 2p orbitals can diminish the bandgap energy and enhance the transplantation of photogenerated carriers, thus hindering the recombination of photogenerated carriers as well as fostering a more conducive environment for photocatalytic oxidation reduction processes [50,51].

Han et al. [52] synthesized BiOCl nanosheets exposing (001) and (110) facets through the solvent thermal method. These nanosheets featured a smooth quadrilateral structure with side lengths ranging from 2 to 4.5 μm (Figure 5b). During the visible-light-induced degradation of phenol over 120 min, approximately 44% degradation was achieved. This effect was attributed to the internal electric field established along the (001) direction, wherein the (001) facet exhibited a high density of terminal oxygen atoms prone to forming oxygen vacancies. Consequently, the photocurrent response of the BiOCl (001) crystal facet was more pronounced (Figure 5c), indicative of enhanced photocatalytic activity [53].

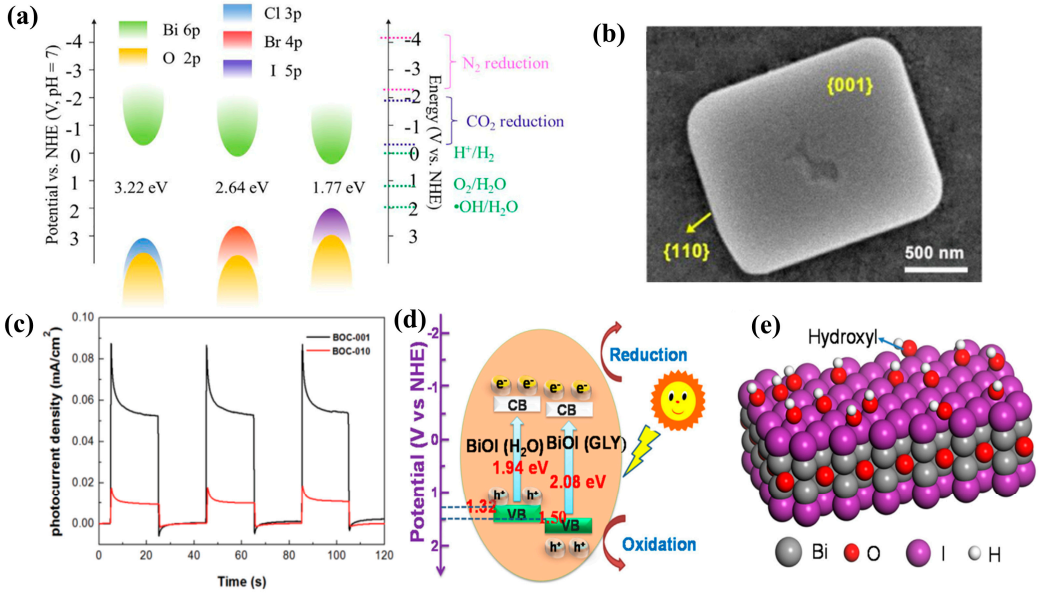

Figure 5. (**a**) Schematic diagram of the CB, VB and band structure of BiOX. Reprinted with permission from Ref. [50]. Copyright 2021 Elsevier. (**b**) SEM image of BiOCl nanosheets with (001) and (110) exposed surfaces. Reprinted with permission from Ref. [52]. Copyright 2021 Elsevier. (**c**) Photocurrent response of BiOCl with different exposed crystal surfaces. Reprinted with permission from Ref. [53]. Copyright 2012 American Chemical Society. (**d**) The schematic of the band structure of BiOI (**e**) Hydroxyl groups adsorbed on the surface of BiOl. Reprinted with permission from Ref. [54]. Copyright 2020 Elsevier.

Wen et al. [55] synthesized BiOBr with varying surface active sites employing different solvents. By transitioning the solvent from water to ethylene glycol, BiOBr featuring Bi vacancies was obtained. The photocatalytic efficacy of materials was evaluated through the visible-light-induced phenol photocatalytic degradation. After two hours, the phenol removal by pure BiOBr was merely 16.5%, whereas over BiOBr containing Bi vacancies, it reached approximately 43.7%. This improvement was attributed to the introduction of Bi vacancy defects that expanded the light absorption spectrum and reduced the carrier recombination rate, thereby boosting the photocatalytic activity. Wang et al. [54] documented the utilization of various organic solvents involved in hydroxyl groups to modulate the surface structure to BiOI photocatalysts. The primary solvents employed included water, n-propanol (NPA), propylene glycol (PG), glycerol (GLY), and meso-erythritol (ME). The visible light photocatalytic performance of BiOI, modulated by various solvents, exceeded that of BiOI (H_2O). Furthermore, the activity of BiOI modulated by glycerol was the most pronounced, achieving an 87% degradation efficiency within three hours. This was illustrated in Figure 5d,e. Hydroxyl groups governed the surface atomic configuration of BiOI nanosheets, inducing a rise in the position of the VBM. Consequently, within the photocatalytic process, a more elevated VBM can facilitate a more potent photogenerated hole oxidation capability compared to the original BiOI.

4. Strategies to Boost the Photocatalytic Performance

This inefficiency for the aforementioned Bi-based catalysts is attributed to the low energy level of the conduction band (CB) and fast reorganization of carriers in single-phase photocatalysts, which hampers efficiency for electron-hole separation and significantly impedes the catalysis under visible light. To enhance the response efficiency under visible light, researchers have explored strategies including structural design and microstructure regulation. This section will discuss the strategies to enhance the photocatalytic efficiency of Bi-based photocatalysts, thereby augmenting photocatalytic activity and achieving a more effective removal of phenol.

4.1. Morphology Control

The efficiency of the catalyst is influenced not only by the chemical composition but also by the particle dimensions and morphology. Generally, photocatalysts with a greater surface area-to-volume ratio demonstrate enhanced photocatalytic efficiency. The reasons are primarily two-fold: first, a larger precise surface region provides additional active sites for reaction; second, on the basis of the formula $\tau = r_0^2/\pi_2 D$ [56], reducing the grain radius can raise the interval efficiency of photogenerated carriers. Therefore, controlling the morphology represents a substantial opportunity to enhance the photocatalytic activity.

Ruan et al. [57] utilized a soft template, β-cyclodextrin, to synthesize oxygen-deficient bismuth tungstate (Bi_2WO_{6-x}) photocatalyst featuring a peony-like morphology by the hydrothermal approach. As depicted in Figure 6a, the SEM image of Bi_2WO_6 reveals a smooth nanosheet morphology with a diameter of 100 to 200 nm and a defined concentration. However, with increasing amounts of β-cyclodextrin, the synthesized Bi_2WO_{6-x} sample transitioned from nanosheets (Figure 6b) to peony-like spheres (Figure 6c) and ultimately to pyknotic spheres (Figure 6d). During a 60 min photocatalytic degradation of phenol, these samples exhibited efficiencies of 16%, 20%, 97%, and 62%, respectively. The layered 3D morphology of Bi_2WO_{6-x} affords multiple active sites, while the plentiful oxygen vacancies facilitate active species generation.

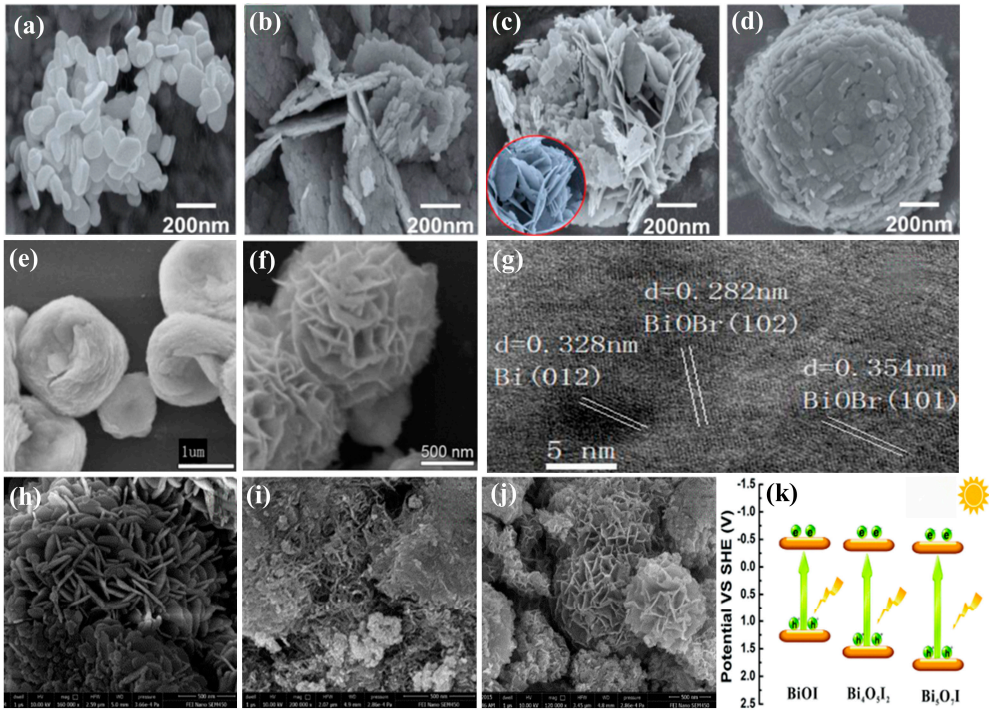

Figure 6. (**a**–**d**) SEM images of Bi_2WO_6 with different morphologies. Reprinted with permission from Ref. [57]. Copyright 2021 Elsevier. (**e**,**f**) SEM image of pure BiOBr and Bi/BiOBr. (**g**) HRTEM images of Bi/BiOBr. Reprinted with permission from Ref. [58]. Copyright 2018 Springer Nature. SEM images of (**h**) BiOI, (**i**) $Bi_4O_5I_2$ and (**j**) Bi_5O_7I. (**k**) the schematic diagram of the band structure of all samples. Reprinted with permission from Ref. [59]. Copyright 2016 Royal Society of Chemistry.

Li et al. [58] developed an improved solvent thermal method to synthesize BiOBr with various morphologies. By introducing a specified amount of $SbCl_3$ into the synthesis system, the reduction of Bi^{3+} to metallic Bi nanoparticles was accelerated, evidently revealing the lattice stripes of metallic Bi and BiOBr in Figure 6g. This process enabled the transformation of layered BiOBr, composed of nanosheets (Figure 6e), into a flower-like microsphere structure (Figure 6f). After 240 min of visible light irradiation, BiOBr and Bi/BiOBr achieved phenol degradation efficiency of 26.4% and 72.9%, respectively. Liu et al. [59] described a

simple mixed solvent method to regulate BiOI with varying iodine contents by aligning the pH of the forerunner solution. Figure 6h–j illustrate that bismuth iodide, with varying oxygen–iodine ratios due to pH changes, yielded different crystal phases of BiOI (tetragonal phase), $Bi_4O_5I_2$ (monoclinic phase), and Bi_5O_7I (orthorhombic phase). They displayed a nanosheet micro-flower shape, an uneven nanosheet shape, and a nanosheet/nanoflower hybrid shape, respectively. In a simulated experiment of the photocatalytic degradation of phenol under visible light, BiOI achieved a photocatalytic efficiency of only 27.6% after 60 min of irradiation, whereas $Bi_4O_5I_2$ and Bi_5O_7I demonstrated significantly higher photocatalytic activities, with a degradation efficiency of 84.2% and 90.1%, respectively. This improvement is attributable to an enhancement in particular surface area and many mesopores during the phase transition process. An increased specific surface area and a greater number of mesopores enhance the adsorption competence and catalytic potency for the material. Furthermore, as demonstrated in Figure 6k, compared to BiOI, $Bi_4O_5I_2$ and Bi_5O_7I feature higher CB positions and lower VB positions. The more negative the CBM and more positive the VB, the greater the oxidation reduction potential for photogenerated carriers [60]. This could be another important factor resulting in the improvement of photocatalytic potency.

4.2. Defect Engineering

Crystal defects are capable of modifying the local electronic and chemical bond characteristics, including the bond length and energy, electronic degrees of freedom, potential defect depth, and the charge and energy density via atomic coordination [61]. Doping is a recognized strategy to enhance the optoelectronic capabilities of materials through the introduction of other ions or defects (Figure 7a,b). Doping primarily comprises two categories: metal doping and non-metal doping [24,62–64]. Under conditions where defects are precisely controlled, substantial modifications to electron dynamics are possible, and even the bandgap and work function of photocatalysts may be tuned [65].

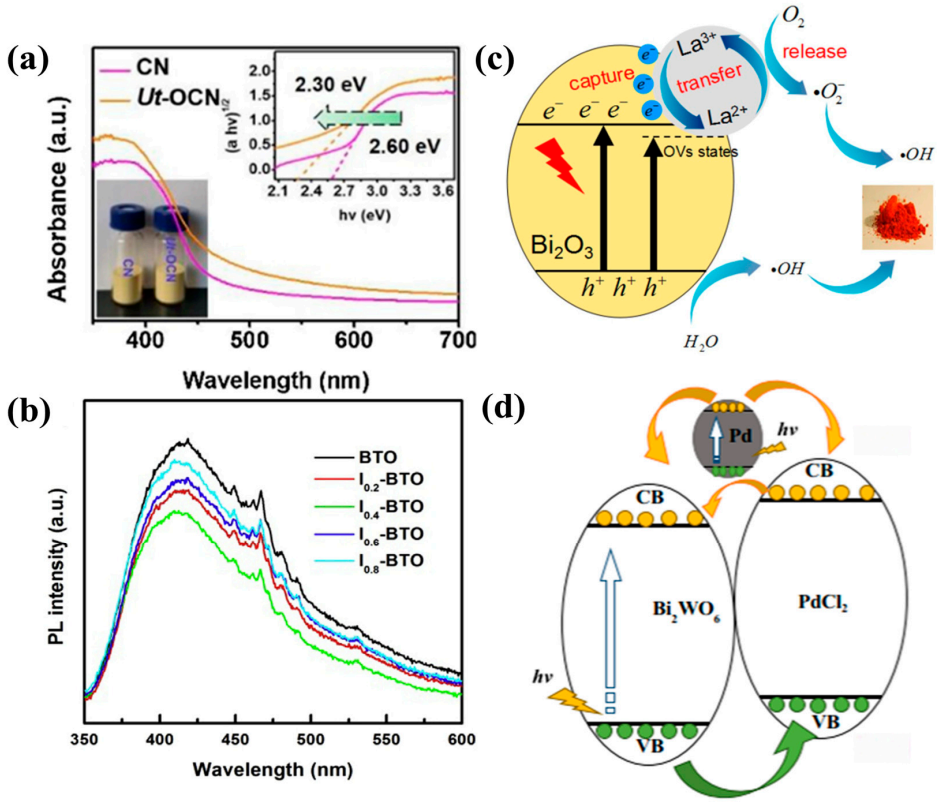

Figure 7. (**a**) UV-Vis diffuse reflectance spectra of CN and Ut-OCN, inset shows the band structure. Reprinted with permission from Ref. [14]. Copyright 2021 Elsevier. (**b**) PL spectra of I-doped $Bi_4Ti_3O_{12}$.

Reprinted with permission from Ref. [66]. Copyright 2022 Elsevier. (**c**) Photocatalytic degradation mechanism of MO by La-Bi_2O_3. Reprinted with permission from Ref. [29]. Copyright 2019 Springer Nature. (**d**) Mechanism of phenol degradation by photocatalyst Pd-Bi_2WO_6. Reprinted with permission from Ref. [67]. Copyright 2018 Elsevier.

4.2.1. Metal Doping

Li et al. [29] synthesized La-doped Bi_2O_3 via a sol–gel approach and induced oxygen vacancies by calcination in an inert atmosphere. Following La doping, the surface of Bi_2O_3 nanosheets becomes roughened, attributed to La^{3+} ions replacing Bi^{3+} in the Bi_2O_3 lattice, forming a Bi-La oxide solid solution. Under visible light irradiation, 2% La-doped Bi_2O_3 achieves a 73% degradation of phenol within 4 h, significantly exceeding the 31% degradation efficiency of pure Bi_2O_3. The enhanced photocatalytic performance of Bi_2O_3 following La doping is attributable to oxygen vacancies, which form an impurity band between the CB and VB, capture photogenerated electrons, and retain more oxidative holes in the VB, thereby facilitating the photocatalytic process. Additionally, as depicted in Figure 7c, La^{3+} ions exhibit remarkable electron scavenging abilities [15], serving as electron capture agents, reacting with O_2 to turn out active free radicals $\cdot O_2^-$, and participating in the oxidation process of phenol.

Meng et al. [67] utilized a photo-reduction technique to dope $Pd/PdCl_2$ on the surface of Bi2WO6, leveraging the surface plasmon resonance (SPR) effect of the precious metal Pd to enhance electron transfer and thereby promote visible light photocatalysis [68]. Thus, 4% Pd-doped Bi_2WO_6 exhibited the highest catalytic performance, achieving 95.2% degradation of phenol within 5 h, significantly exceeding the 60% degradation efficiency of undoped Bi_2WO_6. As illustrated in Figure 7d, for the SPR impression, Pd nanoparticles activated by visible light generate electrons that subsequently transfer to the CB of Bi_2WO_6. Moreover, Pd^0 and Pd^{2+} species on the surface of Bi_2WO_6 effectively enhance the interval of photogenerated carriers by restraining the reorganization of electron-hole pairs.

Liu et al. [41] synthesized Eu^{3+} doped Bi_2MoO_6 nanosheets via a one-pot hydrothermal calcination process. Following doping, due to the smaller radius of Eu^{3+} ions compared to Bi^{3+} ions, lattice contraction occurs, reducing the crystal size of Bi_2MoO_6 and increasing the number of photocatalytic active sites. After 180 min of light irradiation, Bi_2MoO_6 doped with 2% Eu exhibited a phenol degradation efficiency of 97%, significantly surpassing the 40% degradation efficiency of undoped Bi_2MoO_6. This enhancement is attributed to Eu^{3+} doping, which increases visible light absorption and serves as an electron capture site, facilitating the separation of photogenerated carriers and thereby boosting photocatalytic performance.

4.2.2. Non-Metal Doping

In addition to metal element doping, non-metal element doping also enhances photocatalytic performance. Jiang et al. [16] employed NH_4F as a fluoride source and olivine-like $BiVO_4$ as a precursor to synthesize F-doped $BiVO_4$ with a stomatal configuration using a secondary hydrothermal method. With increasing doping levels of F ions, the bandgap of $BiVO_4$-F gradually narrows, enhancing its response to visible light. During a 2 h photocatalytic degradation test of phenol, $BiVO_4$ doped with 0.29F exhibited the highest photocatalytic efficiency, achieving a degradation efficiency of 97%, surpassing the 87% efficiency observed on undoped $BiVO_4$.

In summary, based on the first-principles DOS properties, element doping primarily induces intermediate states within the bandgap or alters the electronic orbital structure, thereby enhancing the photocatalytic activity [69]. Furthermore, the type, quantity, and valence state of doping elements significantly influence the band structure and electronic properties for samples, thereby enhancing both the separation and transfer efficiencies of photogenerated carriers, eventually improving the efficiency of the photocatalyst [61,70].

5. Types of Semiconductor Heterojunctions

The construction of heterojunctions has been demonstrated to efficiently separate photogenerated carriers, establishing it as the most efficacious approach for building high-efficiency photocatalysts [71,72]. Heterojunctions are classified into two major categories. The first category, based on the primary carrier type within the semiconductor, includes p-n junctions, p-p junctions, and n-n junctions. The second category, determined by the band position of the semiconductor, comprises straddling gap type (Type I), staggered gap type (Type II), and broken gap type (Type III).

5.1. p-n Junctions, p-p Junctions, and n-n Junctions

For n-type semiconductors, the primary active species are electrons, whereas in p-type semiconductors, they are holes. As depicted in Figure 8a, two semiconductor types form a representative p-n junction. Upon contact entre p-type and n-type semiconductors, the interface charge transfer mechanism results in a high free electron concentration in the n-area near the junction. Consequently, negatively charged unbound electrons spread abroad the n-type to the p-type semiconductor, where the electron concentration is lower [73]. This diffusion results in the p-n junction carrying a negative charge on the p-region aspect and a positive charge on the n-region side. Diffusion continues until the Fermi energy levels for two materials counterweigh. The regions adjacent to the interface containing positive (n-type material) and negative (p-type material) charges form the depletion layer, where characteristic charge carriers are depleted [74]. A potential difference across the depletion layer forms an IEF extending from the positive to the negative charge regions. As light irradiates the p-n junction, the IEF accelerates the migration of photogenerated electrons from the CB of the p-type to the n-type semiconductor, and of holes from the VB of the n-type to the p-type semiconductor [75,76]. This effective separation of photogenerated carriers increases the photocatalytic performance.

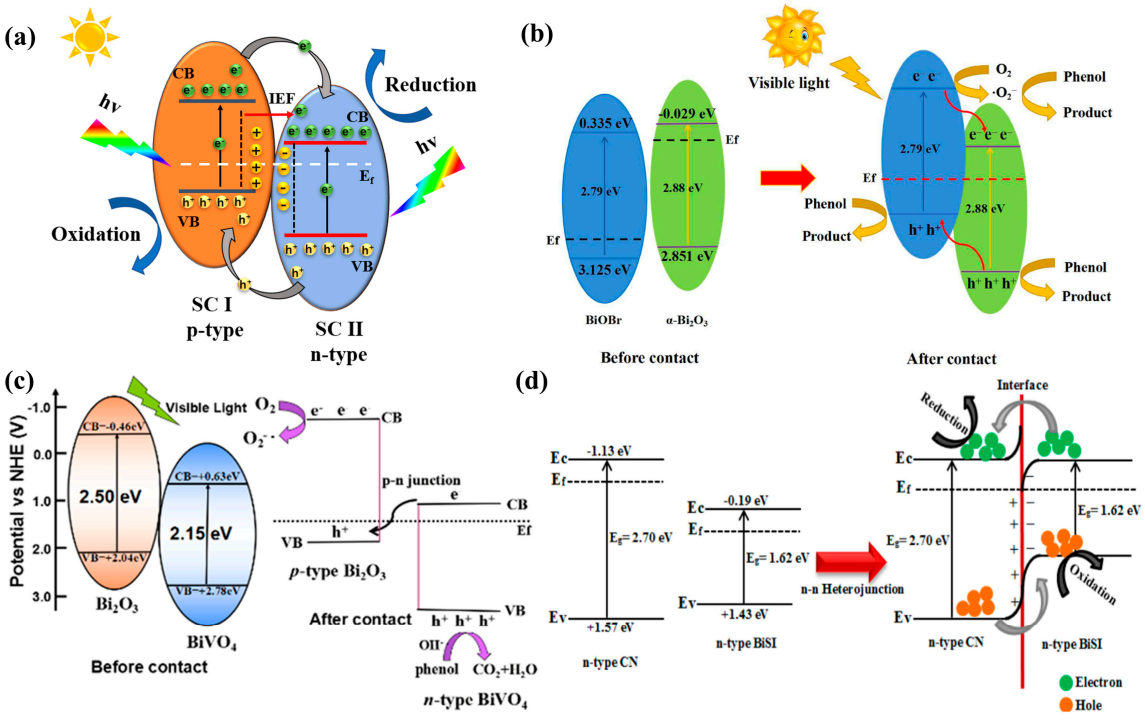

Figure 8. (**a**) Schematic diagram of a typical p-n heterojunction. (**b**) Schematic photo-degradation of phenol by p-BiOBr/n-α-Bi_2O_3 heterojunction. Reprinted with permission from Ref. [30]. Copyright 2023 Elsevier. (**c**) Z-type electron and hole transfer modes in Bi_2O_3-$BiVO_4$ heterojunction. Reprinted with permission from Ref. [17]. Copyright 2016 Elsevier. (**d**) Mechanism of phenol photo-degradation by n-n type CN/BiSI heterojunction. Reprinted with permission from Ref. [19]. Copyright 2022 Elsevier.

Meng et al. [30] synthesized BiOBr/α-Bi_2O_3 p-n heterojunctions by combining the parallel flow precipitation process with the in situ transformation strategy. The optimal composite ratio of BiOBr/α-Bi_2O_3 (BiOBr-70 wt%) showed the highest performance for photocatalytic phenol degradation, achieving a 92.3% removal after visible light irradiation for 60 min, which is 4.44-times and 3.83-times faster than the single-component α-Bi_2O_3 and BiOBr, respectively. As depicted in Figure 8b, the Fermi energy levels of the p-type BiOBr and the n-type α-Bi_2O_3 align closely with their respective VB and CB [30]. According to previous analysis, free electrons spontaneously flow from α-Bi_2O_3 to BiOBr, forming an internal electric field. Upon light excitation, electrons diffuse from the CB of BiOBr to the CB of α-Bi_2O_3, and simultaneously, generated holes migrate from the VB of α-Bi_2O_3 to the VB of BiOBr. This separation effectively enhances the photocatalytic degradation of phenol. Mao et al. [17] utilized a solvothermal method to compound a p-n type porous Bi_2O_3-$BiVO_4$ composite micro-rod semiconductor heterojunction. As for visible light radiation, removing phenol can reach 96.3% after 1 h. Remarkably, the phenol degradation efficiency of pure $BiVO_4$ and Bi_2O_3 is 192- and 160-times higher, respectively. Since $\cdot O_2^-$ is a major active species in phenol degradation and the potential of $BiVO_4$'s CB is below the standard reduction potential of $\cdot O_2^-$ (−0.33 eV), it cannot produce $\cdot O_2^-$. Consequently, the Bi_2O_3-$BiVO_4$ heterojunction does not conform to the conventional p-n junction double-charge transfer mode. Therefore, they proposed a direct Z-type electron and hole diversion mode [71,77] shown in Figure 8c, which is different from the findings of Meng et al. [30]. Upon the light incentive of $BiVO_4$, electrons migrate from the VB to the CB, and simultaneously, some electrons shake up with holes generated in the VB of Bi_2O_3. Subsequently, electrons in the CB of Bi_2O_3 react chemically adsorbed O_2 to induce $\cdot O_2^-$ and in concert with the holes in $BiVO_4$, thus facilitating the oxidation of phenol.

Except for the commonly discussed p-n junctions, there are two types of homojunctions: n-n and p-p heterojunctions. Ji et al. [78] synthesized a flaky n-n type BiOCl/perylene diimide (PDI) heterojunction via a water bath heating method. The absorption margin for BiOCl is at 360 nm; after secondary self-assembly with PDI, the light absorption spectrum of BiOCl/PDI extends to 732 nm, demonstrating enhanced visible light absorption. During a 4 h photocatalytic degradation trial of phenol, BiOCl/PDI achieved a 62% degradation efficiency, 1.4- and 14.6-times higher than that of PDI and BiOCl, respectively. Clusters of PDI encase BiOCl, and since the CB of BiOCl is inferior to that of PDI [18,79], photogenerated electrons transfer from PDI's CB to BiOCl's CB. This facilitates the distance of electrons and holes, thereby enhancing photocatalytic performance. Cao et al. [19] synthesized a binary n-n type CN/BiSI heterojunction via a hydrothermal strategy. At visible light irradiation, 98.8% of phenol degrades within 80 min, significantly exceeding the degradation efficiency of 41.2% for CN and 43.3% for BiSI, respectively. As depicted in Figure 8d, the Fermi level of CN is higher than that of BiSI. When in contact, electrons transfer from CN to BiSI, leading to the formation of an IEF at their boundary surface. Following photoexcitation, the internal electric field facilitates electron diversion from the conduction band of BiSI to that of CN, and hole diversion from the VB of CN to that of BiSI. This enhances the interval of electron holes, thereby improving the photocatalytic degradation of phenol under visible light.

Wang et al. [62] utilized a one-step solvent thermal strategy to synthesize a p-p Z-type BiOBr/$Bi_{12}O_{17}Br_2$ heterojunction, comprising bismuth oxybromide and oxygen-rich bismuth oxybromide. Under irradiation with a 365 nm light source, the degradation efficiency of sulfamethoxazole reached 99%, approximately 13-times and 1.5-times higher than that of BiOBr and $Bi_{12}O_{17}Br_2$, respectively. Differently, the VB potentials of BiOBr and $Bi_{12}O_{17}Br_2$ are 2.01 eV and 1.84 eV, respectively. The standard oxidation potential of hydroxyl radicals ($OH^-/\cdot OH$), a key active species, is 1.99 eV. Consequently, the holes in the valence band of $Bi_{12}O_{17}Br_2$ cannot react with OH^- to produce ·OH, indicating that the p-p junction does not conform to the double-charge transfer mode. Given that the VB potential of BiOBr exceeds the standard oxidation potential of ·OH, electrons from the CB of BiOBr reform with holes in the VB of $Bi_{12}O_{17}Br_2$. Holes in BiOBr's VB react with OH^-

to form ·OH, while electrons in $Bi_{12}O_{17}Br_2$'s CB react with O_2 to form $\cdot O_2^-$. Both ·OH and $\cdot O_2^-$ serve as major active species in promoting the degradation of sulfamethoxazole.

5.2. Type I-III

Schematic diagrams of the three types of second-class heterojunction systems are depicted in Figure 9a–c. In Figure 9a, for the straddling gap-type (Type I) heterojunction, the CB and VB of semiconductor II (SC II) are situated between those of semiconductor I (SC I). In this configuration, photogenerated electrons and holes transfer from the CB and VB of SC I to those of SC II, respectively, where reduction and oxidation reactions predominantly occur. The amassing of electrons and holes in SC I's CB and VB limits charge separation between the semiconductor materials. Simultaneously, the lower redox potential of SC II diminishes the heterojunction's redox capability. These limitations result in low activity for this type of heterojunction semiconductor. Xing et al. [63] prepared $Bi_5Ti_3FeO_{15}$ film by the sol–gel method, and then a $Bi_5Ti_3FeO_{15}$/BiOCl heterojunction was obtained by washing with HCl. The narrow bandgap of $Bi_5Ti_3FeO_{15}$ (2.05eV) and wide bandgap of BiOCl (3.4eV) formed the type I heterojunction. It can shift the flow orientation of the photocharge through ferroelectric polarization, breaking the boundary energy barrier limit of type I heterojunction and forming a type II heterojunction. For the AgI/BiOI/$BiPO_4$ catalyst [64], during the 38 min light reaction process, it can photocatalytically degrade 92.7% of the endocrine disruptor 17α-ethinylestradiol (EE2). This enhancement is due to the constitution of a ternary n-p-n heterojunction comprising n-$BiPO_4$, p-BiOI, and n-AgI, which renders the charge transfer more flexible and promotes the photocatalytic reaction. Overall, for straddling gap heterojunctions, given the limited compatibility and narrow operational range of the two semiconductors, efforts to enhance photocatalytic activity increasingly focus on the construction of p-n junctions.

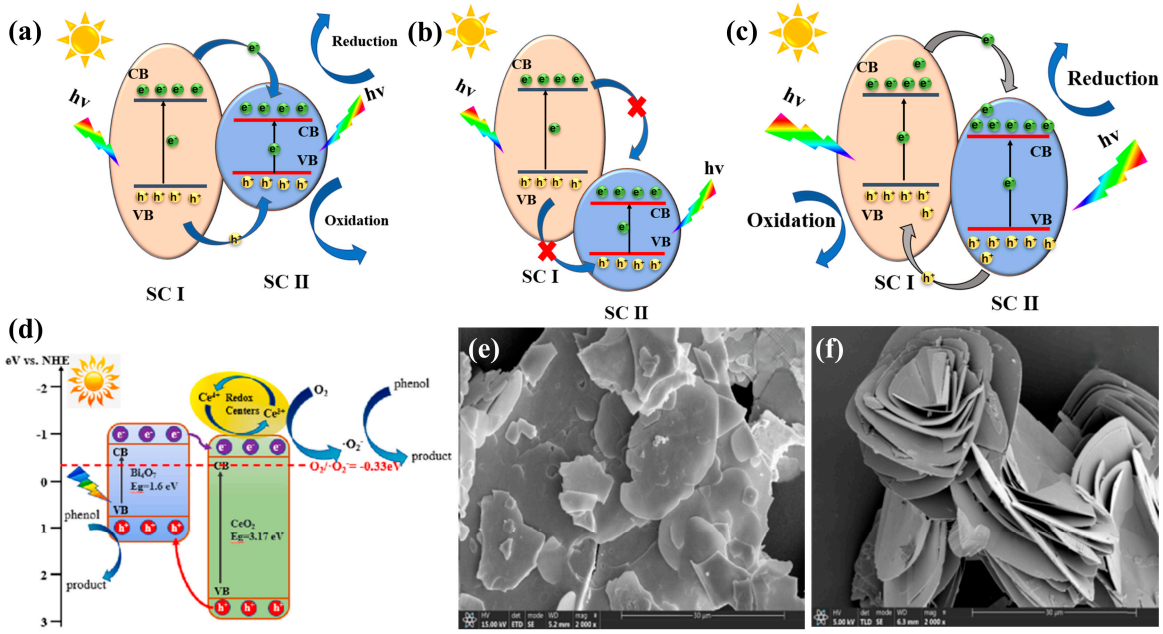

Figure 9. Class II heterojunctions by energy band position: (**a**) I type, (**b**) III type and (**c**) II type. (**d**) Schematic diagram of photocatalytic mechanism for CeO_2/Bi_4O_7 heterojunction. Reprinted with permission from Ref. [20]. Copyright 2022 Elsevier. SEM morphology of BiOI/Bi_5O_7I with 0% (**e**) and 8% (**f**) WHP template addition. Reprinted with permission from Ref. [80]. Copyright 2021 Elsevier.

A schematic diagram of the broken gap-type (Type III) heterojunction is depicted in Figure 9b. In this configuration, the band energy levels of the constituent materials are significantly distant, impeding the diversion of photogenerated carriers between the two semiconductors [81]. Specifically, photogenerated electrons in the CB of SC I cannot

migrate to the CB of SC II, nor can holes in the VB of SC II transfer to the VB of SC I. Consequently, this energy alignment does not support the injection of electrons from SC II's CB into SC I's VB. As a result, each semiconductor functions independently in the photocatalytic process, and physical contact does not enhance the photocatalytic activity. Furthermore, contact between the materials may reduce the surface area or exposure of active photocatalytic sites, decreasing the photocatalytic efficiency [82]. As depicted in Figure 9c, the heterojunction of the staggered gap type manifests superior performance, attributable to its structural design that fosters rapid charge separation and circumvents electron-hole recombination [83]. This, in turn, augments the velocity of redox reactions occurring on the surface of the heterojunction photocatalyst. Within this system, the CB and VB of SC I possess elevated redox potentials at the side of those of SC II. This phenomenon expedites the transference of photoexcited electrons from the CB of SC I to that of SC II, and holes from the VB of SC II to that of SC I. Consequently, this results in the accumulation of reductive electrons in SC II's CB and oxidative holes in SC I's VB, thereby accomplishing the successful interval of photogenerated carriers [84]. Subsequently, reduction reactions predominantly transpire on the external of SC II, while oxidation reactions occur on the external of SC I.

Wang et al. [20] synthesized a type II CeO_2/Bi_4O_7 heterojunction photocatalyst using the hydrothermal method. This photocatalyst exhibited optimal phenol degradation activity when the CeO_2 composite amount was 10%, achieving 92% phenol degrading under visible light irradiation within 120 min. The efficiency of degradation is approximately 7.67- and 2.3-times faster than that of CeO_2 and Bi_4O_7, respectively. The proposed mechanism for phenol degradation, as shown in Figure 9d, involves the conversion of electrons from the VB of CeO_2 and Bi_4O_7 to their respective CBs upon photoexcitation, leading to holes in the VB. Considering that the CB of Bi_4O_7 is more negative, electrons in Bi_4O_7's CB tend to migrate to the CB of CeO_2. Simultaneously, Ce^{4+} in CeO_2 can capture electrons and be reduced to Ce^{3+} [85], combining with O_2 to produce $\cdot O_2^-$ [86], thereby co-oxidizing and degrading phenol with h^+.

Liao et al. [80] reported the preparation of a defective $BiOI/Bi_5O_7I$ heterojunction photocatalyst using the conventional hydrothermal method aided by a water hyacinth powder (WHP) biomaterial template. With an 8% WHP addition, the sample exhibited optimal photocatalytic activity, degrading 70% of phenol under visible light irradiation within five hours, while for no WHP addition, the degradation was only 30%. As illustrated in Figs. 10e and 10f, the use of a water hyacinth powder biomaterial template can cause the self-assembly of BiOI nanoplates into a 3D flower-like structure during the growth of BiOI [87], which is beneficial for the adsorption of the pollutant. Its photocatalytic mechanism resembles that of a type II heterojunction. Notably, due to the presence of defect oxygen vacancies, not only can photogenerated electrons be captured but new energy levels can also be manufactured in the bandgap of BiOI and Bi_5O_7I, thereby better activating molecular oxygen and facilitating the reaction with photogenerated electrons to form $\cdot O_2^-$, which participates in phenol degradation.

5.3. Z-Scheme

The Z-scheme system represents a novel and efficient type of heterojunction, characterized by a band structure like that of a type II heterojunction, albeit with a distinct migration path for photogenerated carriers (Figure 10). Owing to the electron migration path that resembles the letter 'Z', this heterojunction structure is termed a Z-scheme system. Depending upon the presence or shortage of a medium, the Z-scheme system can be further classified into three types: the redox pair medium type, the direct Z-scheme (without a medium), and the solid medium type [88,89]. Bard [90] proposed the redox pair medium Z-scheme in 1979, comprising two different semiconductor photocatalysts and paired electron donor (D) and acceptor (A) ions in an electrolyte solution, as shown in Figure 10a. Holes from the VB of SC II oxidize the D species to A species, while electrons in the CB of SC I reduce the A species to D species. SC I and SC II are not in direct contact with each

other, and photogenerated carriers are transmitted through a reversible redox medium, which acts as an electron transport chain. However, the operational stability and activity of the redox medium gradually decline with long-term use, thereby decreasing the catalytic performance. In comparison, the direct Z-scheme type without the medium demonstrates superior stability. As shown in Figure 10b, upon excitation, these types of heterojunctions generate electrons and holes in their respective CB and VB. However, the photogenerated electrons in the CB of SC II can migrate to the VB of SC I and recombine with the photogenerated holes therein. This electron transport pathway not only facilitates the separation of electron-hole pairs within each semiconductor but also ensures that the electrons in the CB of SC I and the holes in the VB of SC II maintain their highest and original redox potentials, thereby overcoming the shortcomings of type II heterojunctions. Naturally, when the two semiconductors are in immediate contact, it becomes essential for researchers to demonstrate that the material they have prepared is not a type II heterojunction but a direct Z-scheme system.

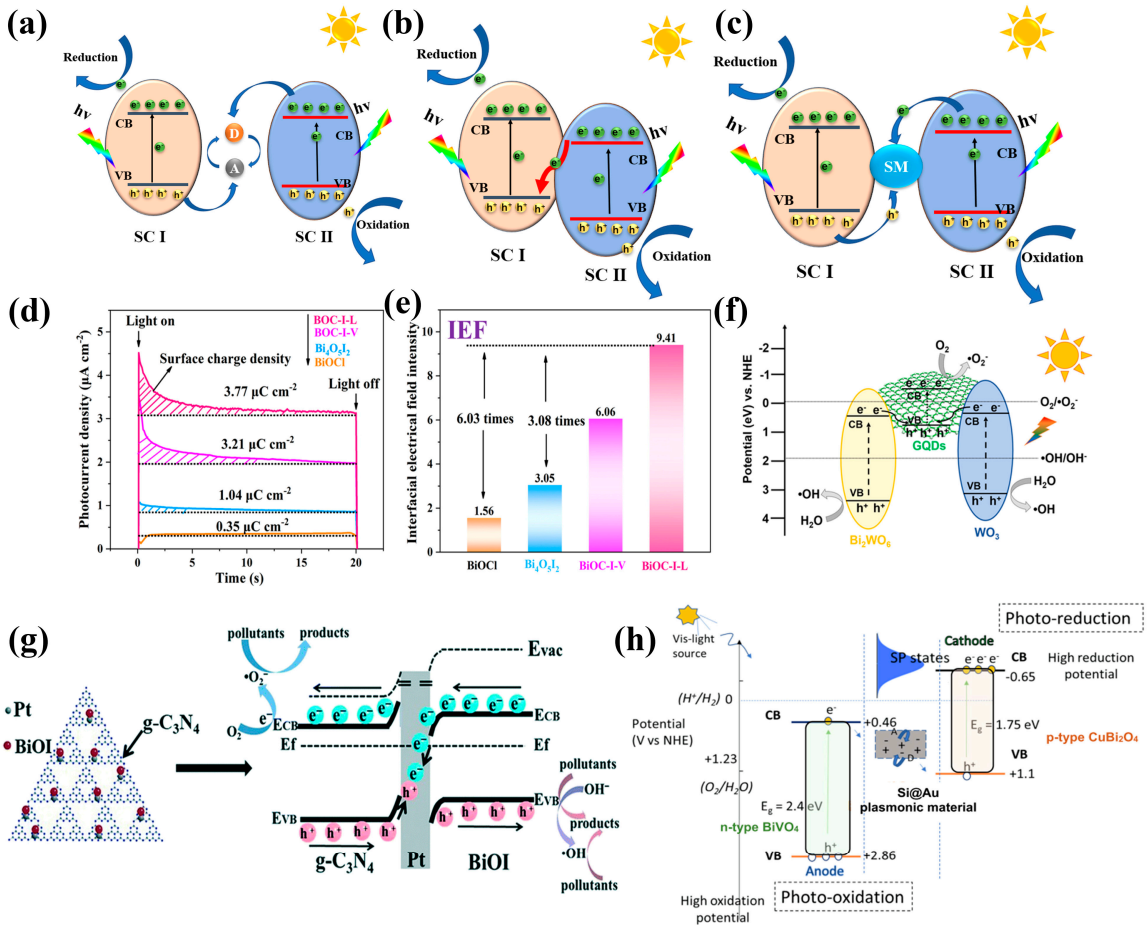

Figure 10. Schematic diagram of electron-hole separation in a Z scheme heterojunction: (**a**) redox pair mediator. (**b**) Direct Z scheme. (**c**) Solid-state dielectric type. The surface charge density (**d**) and the interfacial electric field intensity (**e**) of BiOCl, $Bi_4O_5I_2$, BOC-I-V heterojunction, BOC-I-L heterojunction. Reprinted with permission from Ref. [21]. Copyright 2023 Elsevier. (**f**) Schematic diagram of dual Bi_2WO_6/GQDs/WO_3 Z-scheme photocatalyst. Reprinted with permission from Ref. [91]. Copyright 2020 Elsevier. American Chemical Society. (**g**) The photodegradation mechanism of phenol over all solid-state Z scheme BiOI/Pt/g-C_3N_4 photocatalysts. Reprinted with permission from Ref. [92]. Copyright 2020 Royal Society of Chemistry. (**h**) Diagram of possible mechanism of phenol degradation by Z-type CBO/BVO heterojunction photocatalysts with Si@Au acting as solid-state medium. Reprinted with permission from Ref. [93]. Copyright 2021 Elsevier.

Zhong et al. [21] synthesized two types of two-dimensional $BiOCl/Bi_4O_5I_2$ heterojunction photocatalysts via the hydrothermal method. These include lateral heterojunctions (LHs) formed by chemical bonds and vertical heterojunctions (VHs) formed by van der Waals forces, representing Z-scheme heterojunctions and type II heterojunctions, respectively. At visible light irradiation for 180 min, the two $BiOCl/Bi_4O_5I_2$ heterojunctions achieved phenol degradation efficiency of 98% and 95%, respectively. Although the degradation efficiencies are similar, the phenol degradation efficiency of $BiOCl/Bi_4O_5I_2$-LHs is approximately 2.1-times that of $BiOCl/Bi_4O_5I_2$-VHs. As shown in Figure 10d,e, compared to the $BiOCl/Bi_4O_5I_2$-VHs heterojunction, the $BiOCl/Bi_4O_5I_2$-LHs heterojunction, based on direct chemical bonds, exhibits a higher surface charge density. Therefore, it possesses a stronger internal electric field, and under the Z-scheme model, it facilitates faster photogenerated carrier transfer, a more direct carrier channel, and exhibits the highest photocatalytic activity. Duan et al. [94] synthesized $CuO/CNT/Bi_2WO_6$ composite materials via the solvothermal method, and the catalyst exhibited the capability of degrading approximately 60% of phenol within 2.5 h. The enhancement of its photocatalytic effect is ascribed to the formation of a Z-scheme heterojunction, which promotes the interval of photogenerated electron-hole pairs. Zhou et al. [91] employed electrostatic attraction to uniformly anchor graphene quantum dots on a reverse protein skeleton of Bi_2WO_6/WO_3, and a dual Z-scheme photocatalyst was obtained. The phenol degradation efficiency over $0.5Bi_2WO_6/GQDs/WO_3IO$ reached 99.8% within 120 min, which is 2.8-times higher than that of single WO_3IO. As shown in Figure 10f, the VB of GQDs is close to the CB of Bi_2WO_6 and WO_3. After photoexcitation, the electrons (e^-) in the CB of Bi_2WO_6 and WO_3 recombine with the holes (h^+) in the VB of GQDs. This promotes the reaction of electrons and holes in other parts with O_2 and H_2O to produce active species $\cdot O_2^-$ and $\cdot OH$, thereby facilitating the oxidative removal of phenol.

Although the direct Z-type system effectively enhances the photocatalytic activity through the reorganization of photogenerated electrons from the CB of SC II and vacancies from the VB of SC I at the interface, photocarrier transport capability at this interface deteriorates due to diminished contact compactness or recombination of charge carriers within the components. Consequently, it is imperative to develop a novel system that conveys photogenerated carriers between interfaces more stably and expeditiously. As shown in Figure 10c, this all-solid-state Z-type system contains two distinct semiconductors and a solid electron medium in contact with the interfaces of these semiconductors. This medium typically comprises precious metals such as gold (Au), silver (Ag), and platinum (Pt). Jiang et al. [92] fabricated an all-solid-state Z-type $BiOI/Pt/g\text{-}C_3N_4$ heterojunction photocatalyst using a two-step method. The degradation efficiency of phenol can reach 71.2% under visible light within 120 min, significantly enhancing the phenol degradation efficiency compared to those of single $g\text{-}C_3N_4$, $BiOI/g\text{-}C_3N_4$, and $Pt/g\text{-}C_3N_4$ at 13.6%, 30.2%, and 40.1%, respectively. An elementary diagram of its photocatalytic degradation of phenol is shown in Figure 10g. Compared to the Z-type binary heterojunction, utilizing precious metal Pt as the electron channel enhances carrier transfer efficiency, maximizes charge separation at a zero Schottky barrier, and optimizes oxidation capacity.

Raizada et al. [95] reported a ternary BiOBr/PSCN/Ag/AgCl nano photocatalyst featuring a double Z-scheme, which facilitates the distance of photogenerated electrons and holes through the SPR [96] influence mediated by precious metal Ag. After visible light irradiation for 60 min, it can degrade 98% of phenol, demonstrating lofty photocatalytic performance comparison with bare BiOBr, phosphorus sulphur co-doped graphitic carbon nitride (PSCN), and AgCl. Toe et al. [93] designed a core–shell structured Si@Au-modified $CuBi_2O_4/BiVO_4$ heterojunction photocatalyst. As shown in Figure 10h, the Au layer in the Si@Au core–shell structure achieves surface passivation and suppresses the photoluminescence of Si NP. Simultaneously, as a plasmonic material, it adjusts the SPR effect to enhance the photocatalytic reaction on $CuBi_2O_4/BiVO_4$. The photocatalytic performance of $Si@Au/CuBi_2O_4/BiVO_4$ for phenol degradation, tested under visible light, achieved a degradation efficiency of 96% within 3 h, compared to 57% for $CuBi_2O_4/BiVO_4$ alone. This

efficiency is due to the Fermi level of Au, positioned between the VB of $CuBi_2O_4$ and the CB of $BiVO_4$, acting as a bridge for electron-hole recombination, thus enhancing the utilization within the bands. This further increases the photocatalytic activity of the $CuBi_2O_4/BiVO_4$ heterojunction semiconductor. In summary, this Z-type carrier transport mode, mediated by precious metals, leverages the SPR effect to enhance the virtue of photogenerated carrier separation, thereby boosting the photocatalytic activity.

6. Summary and Outlook

This review comprehensively discusses the photocatalytic degradation of phenol over Bi-based polyoxide catalysts. Based on a brief overview of the basic structure and properties of Bi-based oxides, different kinds of Bi-based oxide catalysts and their catalytic performance are summarized. Subsequently, the effects of morphology, elemental doping, defect introduction, and the band structure on the catalytic performance of Bi-based multi-element oxides are discussed. Aiming to efficiently separate photogenerated electron-hole pairs, various heterojunctions are constructed to develop new Bi-based photocatalysts, thereby achieving efficient phenol removal. Undoubtedly, the layered structure of the Bi-based multi-element oxide photocatalyst offers more active sites for the photocatalytic degradation of phenol, and constructing a Bi-based semiconductor heterojunction maximizes its conduction and valence band redox capabilities, thus significantly enhancing its photocatalytic activity.

Although some valuable results have been obtained, Bi-based oxide photocatalysts still encounter various challenges. For instance, in single-component Bi-based semiconductors, precisely controlling the morphology, exposing high-activity crystal facets, and designing mesoporous structures present significant research value. Regarding new composite materials, identifying materials that match the band structure of Bi-based multi-element oxides and can effectively form heterojunctions offers broad prospects. It is noteworthy that constructing such heterojunction composite structures not only holds potential in photocatalytic pollutant degradation but also in energy applications like hydrogen production and CO_2 reduction.

Author Contributions: Writing original draft paper, Z.L. (Zhangpei Liu); writing—review and editing, M.Q., X.C. and Z.L. (Zhiming Liu); funding acquisition, Z.L. (Zhiming Liu). All authors have read and agreed to the published version of the manuscript.

Funding: This research was funded by the Fundamental Research Funds for the Central Universities (Grant Number: JD2110).

Data Availability Statement: Not applicable.

Conflicts of Interest: The authors declare no conflicts of interest.

References

1. Ranjan, M.; Singh, P.K.; Srivastav, A.L. A review of bismuth-based sorptive materials for the removal of major contaminants from drinking water. *Environ. Sci. Pollut. Res. Int.* **2020**, *27*, 17492–17504. [CrossRef]
2. Wang, J.; Wang, X.; Zhao, G.; Song, G.; Chen, D.; Chen, H.; Xie, J.; Hayat, T.; Alsaedi, A.; Wang, X. Polyvinylpyrrolidone and polyacrylamide intercalated molybdenum disulfide as adsorbents for enhanced removal of chromium(VI) from aqueous solutions. *Chem. Eng. J.* **2018**, *334*, 569–578. [CrossRef]
3. Guo, C.; Tan, Y.; Yang, S.; Qian, Y. Development of phenols recovery process with novel solvent methyl propyl ketone for extracting dihydric phenols from coal gasification wastewater. *J. Clean. Prod.* **2018**, *198*, 1632–1640. [CrossRef]
4. Villegas, L.G.C.; Mashhadi, N.; Chen, M.; Mukherjee, D.; Taylor, K.E.; Biswas, N. A Short Review of Techniques for Phenol Removal from Wastewater. *Curr. Pollut. Rep.* **2016**, *2*, 157–167. [CrossRef]
5. Song, P.; Xu, D.; Yue, J.; Ma, Y.; Dong, S.; Feng, J. Recent advances in soil remediation technology for heavy metal contaminated sites: A critical review. *Sci. Total Environ.* **2022**, *838*, 156417. [CrossRef]
6. Mukherjee, R.; De, S. Novel carbon-nanoparticle polysulfone hollow fiber mixed matrix ultrafiltration membrane: Adsorptive removal of benzene, phenol and toluene from aqueous solution. *Sep. Purif. Technol.* **2016**, *157*, 229–240. [CrossRef]
7. Li, X.; Chang, J.; Zhang, S.; Xiao, L.; Wu, X.; He, Z. Microcystis@TiO_2 Nanoparticles for Photocatalytic Reduction Reactions: Nitrogen Fixation and Hydrogen Evolution. *Catalysts* **2021**, *11*, 1443. [CrossRef]

8. Batra, V.; Kaur, I.; Pathania, D.; Sonu; Chaudhary, V. Efficient dye degradation strategies using green synthesized ZnO-based nanoplatforms: A review. *Appl. Surf. Sci. Adv.* **2022**, *11*, 100314. [CrossRef]
9. Liang, Y.C.; Chou, Y.H. Improved photoelectrode performance of chemical solution-derived Bi_2O_3 crystals via manipulation of crystal characterization. *RSC Adv.* **2020**, *10*, 45042–45058. [CrossRef]
10. Rashmi; Majid, M.; Sivakumar, S. Tetragonal-zircon $BiVO_4$: A better polymorph for the formation of coherent type-II heterostructures for water splitting applications. *Phys. Chem. Chem. Phys.* **2023**, *25*, 27595–27605. [CrossRef] [PubMed]
11. Fu, G.; Xu, G.; Chen, S.; Lei, L.; Zhang, M. Ag_3PO_4/Bi_2WO_6 hierarchical heterostructures with enhanced visible light photocatalytic activity for the degradation of phenol. *Catal. Commun.* **2013**, *40*, 120–124. [CrossRef]
12. Fu, F.; Shen, H.; Sun, X.; Xue, W.; Shoneye, A.; Ma, J.; Luo, L.; Wang, D.; Wang, J.; Tang, J. Synergistic effect of surface oxygen vacancies and interfacial charge transfer on Fe(III)/Bi_2MoO_6 for efficient photocatalysis. *Appl. Catal. B* **2019**, *247*, 150–162. [CrossRef]
13. Gao, P.; Yang, Y.; Yin, Z.; Kang, F.; Fan, W.; Sheng, J.; Feng, L.; Liu, Y.; Du, Z.; Zhang, L. A critical review on bismuth oxyhalide based photocatalysis for pharmaceutical active compounds degradation: Modifications, reactive sites, and challenges. *J. Hazard. Mater.* **2021**, *412*, 125186. [CrossRef]
14. Ma, J.; Jin, D.; Li, Y.; Xiao, D.; Jiao, G.; Liu, Q.; Guo, Y.; Xiao, L.; Chen, X.; Li, X.; et al. Photocatalytic conversion of biomass-based monosaccharides to lactic acid by ultrathin porous oxygen doped carbon nitride. *Appl. Catal. B* **2021**, *283*, 119520. [CrossRef]
15. Ghasemi, S.; Rahimnejad, S.; Setayesh, S.R.; Rohani, S.; Gholami, M.R. Transition metal ions effect on the properties and photocatalytic activity of nanocrystalline TiO_2 prepared in an ionic liquid. *J. Hazard. Mater.* **2009**, *172*, 1573–1578. [CrossRef]
16. Jiang, H.; Dai, H.; Deng, J.; Liu, Y.; Zhang, L.; Ji, K. Porous F-doped $BiVO_4$: Synthesis and enhanced photocatalytic performance for the degradation of phenol under visible-light illumination. *Solid State Sci.* **2013**, *17*, 21–27. [CrossRef]
17. Mao, M.; Chen, F.; Zheng, C.; Ning, J.; Zhong, Y.; Hu, Y. Facile synthesis of porous Bi_2O_3-$BiVO_4$ p-n heterojunction composite microrods with highly efficient photocatalytic degradation of phenol. *J. Alloys Compd.* **2016**, *688*, 1080–1087. [CrossRef]
18. Wang, X.; Wang, Q.; Li, F.; Yang, W.; Zhao, Y.; Hao, Y.; Liu, S. Novel BiOCl–C_3N_4 heterojunction photocatalysts: In situ preparation via an ionic-liquid-assisted solvent-thermal route and their visible-light photocatalytic activities. *Chem. Eng. J.* **2013**, *234*, 361–371. [CrossRef]
19. Cao, Y.; El-Shafay, A.S.; Mohammed, A.H.; Almojil, S.F.; Almohana, A.I.; Alali, A.F. Controlling the charge carriers recombination kinetics on the g-C_3N_4-BiSI n-n heterojunction with efficient photocatalytic activity in N_2 fixation and degradation of MB and phenol. *Adv. Powder Technol.* **2022**, *33*, 103513. [CrossRef]
20. Wang, Y.; Fan, X.; Dong, W.; Zhang, Q.; Liu, J.; Li, R.; Wang, Y.; Zhang, X.; Fan, C. CeO_2 nanoparticles decorated Bi_4O_7 nanosheets for enhanced photodegradation performance of phenol. *Mater. Lett.* **2022**, *322*, 132465. [CrossRef]
21. Zhong, Y.; Wu, C.; Chen, D.; Zhang, J.; Feng, Y.; Xu, K.; Hao, W.; Ding, H.; Lv, G.; Du, Y.; et al. Design of lateral and vertical $Bi_4O_5I_2$/BiOCl heterojunctions with different charge migration pathway for efficient photoredox activity. *Appl. Catal. B* **2023**, *329*, 122554. [CrossRef]
22. Chen, R.; Ren, Z.; Liang, Y.; Zhang, G.; Dittrich, T.; Liu, R.; Liu, Y.; Zhao, Y.; Pang, S.; An, H.; et al. Spatiotemporal imaging of charge transfer in photocatalyst particles. *Nature* **2022**, *610*, 296–301. [CrossRef] [PubMed]
23. Fang, W.; Mi, Y.; Yang, Y.; Jiang, Y.; Liu, Y.; Shangguan, W. Conduction band tuning by strengthening s-p hybridization of novel layered oxyhalide Bi_4SbO_8Cl for efficient visible-light photocatalytic water splitting. *Mater. Today Chem.* **2022**, *26*, 101175. [CrossRef]
24. Liu, Z.; Tai, Y.; Liu, J.; Liu, F.; Han, B.; Fu, W.; Yang, X.; Xie, H.; Liu, Q. A novel mechanism for visible-light degradation of phenol by oxygen vacancy Bi_2MoO_6 homojunction. *Appl. Surf. Sci.* **2022**, *605*, 154671. [CrossRef]
25. Sarkar, R.; Das, D.; Kumar Das, B.; Mitra, A.; Das, N.S.; Sarkar, S.; Chattopadhyay, K.K. Hollow micro-spherical bismuth oxy-chloride for superior visible light induced dye-sensitized photocatalytic activity and its theoretical insight. *Mater. Res. Bull.* **2020**, *125*, 110778. [CrossRef]
26. Tai, Y.; Han, B.; Liu, Z.; Yang, X.; Fu, W.; Gao, R.; Niu, B.; Liu, X.; Zhang, Y.; Liu, Q. Novel core–shell heterojunction photocatalytic wire mesh for efficient ciprofloxacin degradation under visible light. *Sep. Purif. Technol.* **2023**, *306*, 122770. [CrossRef]
27. Li, C.; Chen, G.; Sun, J.; Rao, J.; Han, Z.; Hu, Y.; Xing, W.; Zhang, C. Doping effect of phosphate in Bi_2WO_6 and universal improved photocatalytic activity for removing various pollutants in water. *Appl. Catal. B* **2016**, *188*, 39–47. [CrossRef]
28. Li, Y.; Wang, H.; Huang, L.; Wang, C.; Wang, Q.; Zhang, F.; Fan, X.; Xie, M.; Li, H. Promoting LED light driven photocatalytic inactivation of bacteria by novel β-Bi_2O_3@BiOBr core/shell photocatalyst. *J. Alloys Compd.* **2020**, *816*, 152665. [CrossRef]
29. Li, T.; Quan, S.; Shi, X.; Yang, L.; Liu, C. Fabrication of La-Doped Bi_2O_3 Nanoparticles with Oxygen Vacancies for Improving Photocatalytic Activity. *Catal. Lett.* **2019**, *150*, 640–651. [CrossRef]
30. Meng, Q.; Luo, M.; Jiang, J.; Wan, X. Construction of BiOBr/α-Bi_2O_3 p-n heterojunction as a highly efficacious visible-light-induced photocatalyst for phenol removal. *Vacuum* **2023**, *214*, 112178. [CrossRef]
31. Wu, J.; Ding, B.; Qian, X.; Mao, L.; Zheng, H.; Yang, Y.; Zhang, L.; Zheng, S.; Zhang, J. Sunlight driven isotropic beta-Bi_2O_3 with high charge-carrier mobility for the efficient degradation of bisphenol A and phenol. *Dalton Trans.* **2022**, *51*, 8401–8410. [CrossRef] [PubMed]
32. Meng, X.; Li, Z.; Zhang, Z. Pd-nanoparticle-decorated peanut-shaped $BiVO_4$ with improved visible light-driven photocatalytic activity comparable to that of TiO_2 under UV light. *J. Catal.* **2017**, *356*, 53–64. [CrossRef]

33. Sun, S.; Wang, W.; Xu, J.; Wang, L.; Zhang, Z. Highly efficient photocatalytic oxidation of phenol over ordered mesoporous Bi_2WO_6. *Appl. Catal. B* **2011**, *106*, 559–564. [CrossRef]
34. Uezono, N.; Liu, J.; Pawar, S.A.; Islam, M.M.; Ikeda, S.; Sakurai, T. Crystalline phase control of $BiVO_4$ thin films using RF sputtering. *Jpn. J. Appl. Phys.* **2023**, *62*, SK1001. [CrossRef]
35. Babu, P.; Mohanty, S.; Naik, B.; Parida, K. Serendipitous Assembly of Mixed Phase $BiVO_4$ on B-Doped g-C_3N_4: An Appropriate p–n Heterojunction for Photocatalytic O_2 evolution and Cr(VI) reduction. *Inorg. Chem.* **2019**, *58*, 12480–12491. [CrossRef]
36. Xie, B.; Zhang, H.; Cai, P.; Qiu, R.; Xiong, Y. Simultaneous photocatalytic reduction of Cr(VI) and oxidation of phenol over monoclinic $BiVO_4$ under visible light irradiation. *Chemosphere* **2006**, *63*, 956–963. [CrossRef] [PubMed]
37. Sun, M.; Guo, P.; Wang, M.; Ren, F. The effect of pH on the photocatalytic performance of $BiVO_4$ for phenol mine sewage degradation under visible light. *Optik* **2019**, *179*, 672–679. [CrossRef]
38. Liu, X.; Gu, S.; Zhao, Y.; Zhou, G.; Li, W. $BiVO_4$, Bi_2WO_6 and Bi_2MoO_6 photocatalysis: A brief review. *J. Mater. Sci. Technol.* **2020**, *56*, 45–68. [CrossRef]
39. Xiong, X.; Yang, H.; Zhang, J.; Lin, J.; Yang, S.; Chen, C.; Xi, J.; Kong, Z.; Song, L.; Zeng, J. Novel MoSSe/Bi_2WO_6 S-scheme heterojunction photocatalysts for significantly improved photoelectrochemical and photocatalytic performance. *J. Alloys Compd.* **2023**, *933*, 167784. [CrossRef]
40. Sattari, M.; Farhadian, M.; Reza Solaimany Nazar, A.; Moghadam, M. Enhancement of Phenol degradation, using of novel Z-scheme $Bi_2WO_6/C_3N_4/TiO_2$ composite: Catalyst and operational parameters optimization. *J. Photochem. Photobiol. A* **2022**, *431*, 114065. [CrossRef]
41. Liu, X.; Zhou, W.; Li, F.; Yu, C. Eu^{3+} doped Bi_2MoO_6 nanosheets fabricated via hydrothermal-calcination route and their superior performance for aqueous volatile phenols removal. *J. Taiwan Inst. Chem. Eng.* **2021**, *125*, 276–284. [CrossRef]
42. Sun, M.; Guo, P.; Wang, M.; Ren, F. The effect of calcination temperature on the photocatalytic performance of Bi_2MoO_6 for the degradation of phenol under visible light. *Optik* **2019**, *199*, 163319. [CrossRef]
43. Chang Chien, S.-W.; Ng, D.-Q.; Kumar, D.; Lam, S.-M.; Jaffari, Z.H. Investigating the effects of various synthesis routes on morphological, optical, photoelectrochemical and photocatalytic properties of single-phase perovskite $BiFeO_3$. *J. Phys. Chem. Solids* **2022**, *160*, 110342. [CrossRef]
44. Zargazi, M.; Entezari, M.H. A novel synthesis of forest like $BiFeO_3$ thin film: Photo-electrochemical studies and its application as a photocatalyst for phenol degradation. *Appl. Surf. Sci.* **2019**, *483*, 793–802. [CrossRef]
45. Lam, S.-M.; Jaffari, Z.H.; Sin, J.-C.; Zeng, H.; Lin, H.; Li, H.; Mohamed, A.R. Insight into the influence of noble metal decorated on $BiFeO_3$ for 2,4-dichlorophenol and real herbicide wastewater treatment under visible light. *Colloids Surf. A* **2021**, *614*, 126138. [CrossRef]
46. Yin, J.; Liao, G.; Zhou, J.; Huang, C.; Ling, Y.; Lu, P.; Li, L. High performance of magnetic $BiFeO_3$ nanoparticle-mediated photocatalytic ozonation for wastewater decontamination. *Sep. Purif. Technol.* **2016**, *168*, 134–140. [CrossRef]
47. Sun, X.; Xu, T.; Xian, T.; Yi, Z.; Liu, G.; Dai, J.; Yang, H. Insight on the enhanced piezo-photocatalytic mechanism of $In_2O_3/BiFeO_3$ heterojunctions for degradation of tetracycline hydrochloride. *Appl. Surf. Sci.* **2023**, *640*, 158408. [CrossRef]
48. Mansingh, S.; Sultana, S.; Acharya, R.; Ghosh, M.K.; Parida, K.M. Efficient Photon Conversion via Double Charge Dynamics CeO_2-$BiFeO_3$ p-n Heterojunction Photocatalyst Promising toward N_2 Fixation and Phenol-Cr(VI) Detoxification. *Inorg. Chem.* **2020**, *59*, 3856–3873. [CrossRef]
49. Di, J.; Xia, J.; Li, H.; Guo, S.; Dai, S. Bismuth oxyhalide layered materials for energy and environmental applications. *Nano Energy* **2017**, *41*, 172–192. [CrossRef]
50. Guo, J.; Li, X.; Liang, J.; Yuan, X.; Jiang, L.; Yu, H.; Sun, H.; Zhu, Z.; Ye, S.; Tang, N.; et al. Fabrication and regulation of vacancy-mediated bismuth oxyhalide towards photocatalytic application: Development status and tendency. *Coord. Chem. Rev.* **2021**, *443*, 214033. [CrossRef]
51. Cheng, H.; Huang, B.; Dai, Y. Engineering BiOX (X = Cl, Br, I) nanostructures for highly efficient photocatalytic applications. *Nanoscale* **2014**, *6*, 2009–2026. [CrossRef] [PubMed]
52. Han, Y.; Li, Q.; Bao, S.; Lu, Y.; Guan, Z.; Zhang, J.; Tian, B. Z-scheme heterostructure BiOCl-Ag-AgBr with enhanced sunlight-driven photocatalytic activity in simultaneous removal of Cr^{6+} and phenol contaminants. *Catal. Today* **2021**, *376*, 151–161. [CrossRef]
53. Jiang, J.; Zhao, K.; Xiao, X.; Zhang, L. Synthesis and facet-dependent photoreactivity of BiOCl single-crystalline nanosheets. *J. Am. Chem. Soc.* **2012**, *134*, 4473–4476. [CrossRef]
54. Wang, X.; Zhang, Y.; Zhou, C.; Huo, D.; Zhang, R.; Wang, L. Hydroxyl-regulated BiOI nanosheets with a highly positive valence band maximum for improved visible-light photocatalytic performance. *Appl. Catal. B* **2020**, *268*, 118390. [CrossRef]
55. Wen, R.; Yang, L.; Wu, S.; Zhou, D.; Jiang, B. Tuning surface sites to boost photocatalytic degradation of phenol and ciprofloxacin. *Chin. Chem. Lett.* **2023**, *34*, 107204. [CrossRef]
56. Sun, S.; Wang, W.; Zhang, L. Bi_2WO_6 Quantum Dots Decorated Reduced Graphene Oxide: Improved Charge Separation and Enhanced Photoconversion Efficiency. *J. Phys. Chem. C* **2013**, *117*, 9113–9120. [CrossRef]
57. Ruan, X.; Wen, X.; Liang, D.; Hu, Y. Hierarchically peony-analogous bismuth tungstate with oxygen vacancies for enhanced photocatalytic degradation of phenolic compounds. *J. Clean. Prod.* **2021**, *324*, 129287. [CrossRef]
58. Li, Y.; Zhu, J.; Yang, R.; Shao, M. Facile synthesis of Bi decorated 2D and 3D BiOBr micro-nanostructures with enhanced photocatalytic activity. *Micro Nano Lett.* **2018**, *13*, 1040–1045. [CrossRef]

59. Liu, C.; Wang, X. Room temperature synthesis of $Bi_4O_5I_2$ and Bi_5O_7I ultrathin nanosheets with a high visible light photocatalytic performance. *Dalton Trans.* **2016**, *45*, 7720–7727. [CrossRef]
60. Yang, J.; Xu, L.; Liu, C.; Xie, T. Preparation and photocatalytic activity of porous Bi_5O_7I nanosheets. *Appl. Surf. Sci.* **2014**, *319*, 265–271. [CrossRef]
61. Du, X.; Huang, J.; Zhang, J.; Yan, Y.; Wu, C.; Hu, Y.; Yan, C.; Lei, T.; Chen, W.; Fan, C.; et al. Modulating Electronic Structures of Inorganic Nanomaterials for Efficient Electrocatalytic Water Splitting. *Angew. Chem. Int. Ed. Engl.* **2019**, *58*, 4484–4502. [CrossRef] [PubMed]
62. Wang, F.; Ma, N.; Zheng, L.; Zhang, L.; Bian, Z.; Wang, H. Interface engineering of p-p Z-scheme BiOBr/$Bi_{12}O_{17}Br_2$ for sulfamethoxazole photocatalytic degradation. *Chemosphere* **2022**, *307*, 135666. [CrossRef] [PubMed]
63. Xing, F.; Wang, L.; Zhou, Y.; Jin, S.; Jin, H.; Li, J. Breaking through the interfacial energy barrier limitations of type-I heterojunctions via ferroelectric polarization engineering: A case study of $Bi_5Ti_3FeO_{15}$/BiOCl. *Inorg. Chem. Front.* **2023**, *10*, 3112–3120. [CrossRef]
64. Long, Y.; Li, L.; Zhou, L.; Zhang, S.; Wang, L.; Zheng, Z.; Wu, S.; Hei, Y.; Jiang, F. Fabrication of the AgI/BiOI/$BiPO_4$ multi-heterojunction with high photocatalytic activity. *Mater. Res. Bull.* **2020**, *126*, 110787. [CrossRef]
65. Wang, Z.; Chen, M.; Huang, D.; Zeng, G.; Xu, P.; Zhou, C.; Lai, C.; Wang, H.; Cheng, M.; Wang, W. Multiply structural optimized strategies for bismuth oxyhalide photocatalysis and their environmental application. *Chem. Eng. J.* **2019**, *374*, 1025–1045. [CrossRef]
66. Cheng, T.; Ma, Q.; Gao, H.; Meng, S.; Lu, Z.; Wang, S.; Yi, Z.; Wu, X.; Liu, G.; Wang, X.; et al. Enhanced photocatalytic activity, mechanism and potential application of Idoped-$Bi_4Ti_3O_{12}$ photocatalysts. *Mater. Today Chem.* **2022**, *23*, 100750. [CrossRef]
67. Meng, X.; Qin, H.; Zhang, Z. New insight into the enhanced visible light-driven photocatalytic activity of Pd/$PdCl_2$-doped Bi_2WO_6 photocatalysts. *J. Colloid Interface Sci.* **2018**, *513*, 877–890. [CrossRef]
68. Meng, X.; Zhang, Z. Bi_2MoO_6 co-modified by reduced graphene oxide and palladium ($Pd^{2+}$and Pd^0) with enhanced photocatalytic decomposition of phenol. *Appl. Catal. B* **2017**, *209*, 383–393. [CrossRef]
69. Patnaik, S.; Sahoo, D.P.; Parida, K. Recent advances in anion doped g-C_3N_4 photocatalysts: A review. *Carbon* **2021**, *172*, 682–711. [CrossRef]
70. Meng, X.; Li, Z.; Chen, J.; Xie, H.; Zhang, Z. Enhanced visible light-induced photocatalytic activity of surface-modified BiOBr with Pd nanoparticles. *Appl. Surf. Sci.* **2018**, *433*, 76–87. [CrossRef]
71. Wang, J.C.; Zhang, L.; Fang, W.X.; Ren, J.; Li, Y.Y.; Yao, H.C.; Wang, J.S.; Li, Z.J. Enhanced Photoreduction CO_2 Activity over Direct Z-Scheme alpha-Fe_2O_3/Cu_2O Heterostructures under Visible Light Irradiation. *ACS Appl. Mater. Interfaces* **2015**, *7*, 8631–8639. [CrossRef]
72. Liu, Z.; Cai, L.; Tai, Y.; Deng, J.; Wu, Q.; Zhao, Y.; Xie, H.; Liu, Q. Synergistic Effects of Sulfur Vacancies and Internal Electric Fields in FeS/MoS_2 Heterojunctions: A New Approach to Photocatalytic Chromium Removal. *Chemosphere* **2024**, *364*, 143021. [CrossRef] [PubMed]
73. Jing, Q.; Liu, Z.; Cheng, X.; Li, C.; Ren, P.; Guo, K.; Yue, H.; Xie, B.; Li, T.; Wang, Z.; et al. Boosting piezo-photocatalytic activity of $BiVO_4$/$BiFeO_3$ heterojunctions through built-in polarization field tailoring carrier transfer performances. *Chem. Eng. J.* **2023**, *464*, 142617. [CrossRef]
74. Chen, L.; Ren, J.T.; Yuan, Z.Y. Enabling Internal Electric Fields to Enhance Energy and Environmental Catalysis. *Adv. Energy Mater.* **2023**, *13*, 2203720. [CrossRef]
75. Chen, L.; He, J.; Liu, Y.; Chen, P.; Au, C.-T.; Yin, S.-F. Recent advances in bismuth-containing photocatalysts with heterojunctions. *Chin. J. Catal.* **2016**, *37*, 780–791. [CrossRef]
76. Yu, C.; Zhou, W.; Yu, J.C.; Liu, H.; Wei, L. Design and fabrication of heterojunction photocatalysts for energy conversion and pollutant degradation. *Chin. J. Catal.* **2014**, *35*, 1609–1618. [CrossRef]
77. Lin, J.; He, J.; Hu, J.; Dong, J.; Liu, A.; Yang, Y.; Tang, L.; Li, L.; Zhou, Y.; Zou, Z. In situ construction of a 2D/2D heterostructured $ZnIn_2S_4$/Bi_2MoO_6 Z-scheme system for boosting the photoreduction activity of Cr(vi). *Catal. Sci. Technol.* **2021**, *11*, 3885–3893. [CrossRef]
78. Ji, Q.; Xu, Z.; Xiang, W.; Wu, Y.; Cheng, X.; Xu, C.; Qi, C.; He, H.; Hu, J.; Yang, S.; et al. Enhancing the performance of pollution degradation through secondary self-assembled composite supramolecular heterojunction photocatalyst BiOCl/PDI under visible light irradiation. *Chemosphere* **2020**, *253*, 126751. [CrossRef]
79. Zhang, K.; Wang, J.; Jiang, W.; Yao, W.; Yang, H.; Zhu, Y. Self-assembled perylene diimide based supramolecular heterojunction with Bi_2WO_6 for efficient visible-light-driven photocatalysis. *Appl. Catal. B* **2018**, *232*, 175–181. [CrossRef]
80. Liao, H.; Li, Z.; Luo, L.; Zhong, J.; Li, J. Water hyacinth powder -assisted preparation of defects-rich and flower-like BiOI/Bi_5O_7I heterojunctions with excellent visible light photocatalytic activity. *Surf. Interfaces* **2021**, *27*, 101470. [CrossRef]
81. Marschall, R. Semiconductor Composites: Strategies for Enhancing Charge Carrier Separation to Improve Photocatalytic Activity. *Adv. Funct. Mater.* **2013**, *24*, 2421–2440. [CrossRef]
82. Özçelik, V.O.; Azadani, J.G.; Yang, C.; Koester, S.J.; Low, T. Band alignment of two-dimensional semiconductors for designing heterostructures with momentum space matching. *Phys. Rev. B* **2016**, *94*, 35125. [CrossRef]
83. Jiao, H.; Wang, X.; Chen, Y.; Guo, S.; Wu, S.; Song, C.; Huang, S.; Huang, X.; Tai, X.; Lin, T.; et al. HgCdTe/black phosphorus van der Waals heterojunction for high-performance polarization-sensitive midwave infrared photodetector. *Sci. Adv.* **2022**, *8*, eabn1811. [CrossRef]

84. Li, J.; Chen, J.; Fang, H.; Guo, X.; Rui, Z. Plasmonic Metal Bridge Leading Type III Heterojunctions to Robust Type B Photothermocatalysts. *Ind. Eng. Chem. Res.* **2021**, *60*, 8420–8429. [CrossRef]
85. Xiao, Y.; Tan, S.; Wang, D.; Wu, J.; Jia, T.; Liu, Q.; Qi, Y.; Qi, X.; He, P.; Zhou, M. $CeO_2/BiOIO_3$ heterojunction with oxygen vacancies and Ce^{4+}/Ce^{3+} redox centers synergistically enhanced photocatalytic removal heavy metal. *Appl. Surf. Sci.* **2020**, *530*, 147116. [CrossRef]
86. Kusmierek, E. A CeO_2 Semiconductor as a Photocatalytic and Photoelectrocatalytic Material for the Remediation of Pollutants in Industrial Wastewater: A Review. *Catalysts* **2020**, *10*, 1435. [CrossRef]
87. Li, H.; Chen, Y.; Zhou, W.; Jiang, H.; Liu, H.; Chen, X.; Tian, G. $WO_3/BiVO_4/BiOCl$ porous nanosheet composites from a biomass template for photocatalytic organic pollutant degradation. *J. Alloys Compd.* **2019**, *802*, 76–85. [CrossRef]
88. Low, J.; Yu, J.; Jaroniec, M.; Wageh, S.; Al-Ghamdi, A.A. Heterojunction Photocatalysts. *Adv. Mater.* **2017**, *29*, 1601694. [CrossRef]
89. Xu, Q.; Zhang, L.; Yu, J.; Wageh, S.; Al-Ghamdi, A.A.; Jaroniec, M. Direct Z-scheme photocatalysts: Principles, synthesis, and applications. *Mater. Today* **2018**, *21*, 1042–1063. [CrossRef]
90. Bard, A.J. Photoelectrochemistry and heterogeneous photo-catalysis at semiconductors. *J. Photochem.* **1979**, *10*, 59–75. [CrossRef]
91. Zhou, Q.; Song, Y.; Li, N.; Chen, D.; Xu, Q.; Li, H.; He, J.; Lu, J. Direct Dual Z-Scheme $Bi_2WO_6/GQDs/WO_3$ Inverse Opals for Enhanced Photocatalytic Activities under Visible Light. *ACS Sustain. Chem. Eng.* **2020**, *8*, 7921–7927. [CrossRef]
92. Jiang, J.; Song, Y.; Wang, X.; Li, T.; Li, M.; Lin, Y.; Xie, T.; Dong, S. Enhancing aqueous pollutant photodegradation via a Fermi level matched Z-scheme BiOI/Pt/g-C_3N_4 photocatalyst: Unobstructed photogenerated charge behavior and degradation pathway exploration. *Catal. Sci. Technol.* **2020**, *10*, 3324–3333. [CrossRef]
93. Toe, E.D.; Kurniawan, W.; Andrews, E.M.; Nakasaki, K.; Hinode, H.; Aziz, M. All-solid-state Z-scheme plasmonic Si@Au nanoparticles on $CuBi_2O_4/BiVO_4$ for efficient photocatalytic activity. *Adv. Powder Technol.* **2021**, *32*, 4330–4342. [CrossRef]
94. Duan, J.; Liu, M.; Song, X.; Wang, W.; Zhang, Z.; Li, C. Enhanced photocatalytic degradation of organic pollutants using carbon nanotube mediated CuO and Bi_2WO_6 sandwich flaky structures. *Nanotechnology* **2020**, *31*, 425202. [CrossRef]
95. Raizada, P.; Thakur, P.; Sudhaik, A.; Singh, P.; Thakur, V.K.; Hosseini-Bandegharaei, A. Fabrication of dual Z-scheme photocatalyst via coupling of BiOBr/Ag/AgCl heterojunction with P and S co-doped g-C_3N_4 for efficient phenol degradation. *Arab. J. Chem.* **2020**, *13*, 4538–4552. [CrossRef]
96. Zhou, T.; Xu, Y.; Xu, H.; Wang, H.; Da, Z.; Huang, S.; Ji, H.; Li, H. In situ oxidation synthesis of visible-light-driven plasmonic photocatalyst Ag/AgCl/g-C_3N_4 and its activity. *Ceram. Int.* **2014**, *40*, 9293–9301. [CrossRef]